Computational Materials Science 229 (2023) 112415

Contents lists available at ScienceDirect

Computational Materials Science

journal homepage: www.elsevier.com/locate/commatsci

Full length article

Computationally guided epitaxial synthesis of (Sr/Ba)MnO_3 films on (Sr/Ba)TiO_3 substrates

Catherine Zhou, Gregory S. Rohrer, Paul A. Salvador *

Department of Materials Science and Engineering, Carnegie Mellon University, 5000 Forbes Ave., Pittsburgh, PA 15213, USA

ARTICLE INFO

Keywords:
Density functional theory
Epitaxial thin films
Orientation relationships
Polymorphs
Oxides

ABSTRACT

Density functional theory (DFT) was used in the computation of thermodynamic terms relevant to the competition between epitaxial polytypes during nucleation of (Sr/Ba)MnO_3 on (100), (110), and (111) cubic (Sr/Ba)TiO_3 substrates. Values for volumetric formation energies, volumetric strain energies, and area-specific interface energies were computed for different polytypes ($3C$, $4H$, and $2H$) and were incorporated in a standard (capillarity) model for epitaxial nucleation. Experimental orientation relationships (ORs) for $SrMnO_3$ were used in the construction of strained and interface cells for (Sr/Ba)MnO_3. For $3C$ polytypes, the OR is simply cube-on-cube, or $(111)[1\bar{1}0]_{3C,\ film}||(111)[1\bar{1}0]_{3C,\ sub}$, and is isostructural with cubic (Sr/Ba)TiO_3. For $4H/2H$ polytypes, the orientation relationship is $(001)[100]_{4H/2H,\ film}||(111)[1\bar{1}0]_{3C,\ sub}$, which can only be modeled with a coherent interface on the (111) substrate. Results indicate that $3C$ $SrMnO_3$ has increased energies (becomes less stable) on moving from $SrTiO_3$ substrate orientations (100) to (110) to (111), consistent with experimental observations. For $BaMnO_3$, similar trends are predicted, although no experimental data is available for comparison. We use the DFT results to discuss the different thermodynamic contributions to polytype stability, and assess the feasibility of stabilizing a $3C$ $BaMnO_3$ film on (Sr/Ba)TiO_3 substrates.

1. Introduction

Epitaxial growth is a well-known method to stabilize metastable oxides as thin films [1–5]. However, experimental growth conditions and substrate types that promote epitaxial stabilization are not usually known in advance and determination/optimization of these parameters typically encompasses entire research studies. Additionally, substrate orientation can play an essential role in directing the crystal structure (and orientation) of the film [5–10], which is another factor that is found by trial and error. In order to accelerate the discovery of new materials with novel properties, computational methods are needed that (1) can guide epitaxial growth in the laboratory and (2) are accessible to experimentalists. Many computational studies on metastable perovskite polymorphs focus broadly on bulk stabilities and homoepitaxial strain, which can guide experiments to an extent, but neither approach involves interfaces with specific substrates and orientations [11–14]. Herein, we continue to describe what we call computationally guided epitaxial synthesis, or CGES, which is based on first-principles computations using density functional theory (DFT) as developed by Xu et al. [15] to describe TiO_2 polymorph growth on (Sr/Ba)TiO_3 substrates. Computations of TiO_2 epitaxial stability were consistent with experimental observations and independent of exchange–correlation functionals used. In this paper, we apply CGES to investigate the thermodynamic contributions of volumetric formation energy, strain energy, and interface energy to the nucleation of (Sr/Ba)MnO_3 polytypes on three low Miller index (Sr/Ba)TiO_3 substrate orientations.

To compute strain and interface energy values for films on different substrate orientations, one needs to know the preferred orientation relationship (ORs) between target films and substrates [7,8]. One common preferred OR is called the eutactic OR, which aligns the nearly close-packed (eutactic) planes and directions over all of substrate orientation space. Experimentally, many oxides deposited on polycrystalline substrates are observed to have the eutactic OR as the preferred OR [5–8,16,17]. For $SrMnO_3$ on $SrTiO_3$, Zhou et al. [7,8] found that the eutactic OR was the only OR, regardless of film phase, substrate orientation, or deposition conditions. This suggests that it may be reasonable to assume the eutactic OR for novel oxide thin films on oxide substrates when in search of the best substrate material and orientation using DFT. This greatly decreases the number of required computations for CGES and enables investigations of the sort described here.

In this study of epitaxial polymorph competition, we use the (Sr/Ba)MnO_3 system as a model because these materials can exist in different structures in bulk [18–22]. The different polymorphs are closely related

* Corresponding author.
E-mail address: paulsalvador@cmu.edu (P.A. Salvador).

https://doi.org/10.1016/j.commatsci.2023.112415
Received 17 May 2023; Received in revised form 28 July 2023; Accepted 28 July 2023

by different stacking sequences of SrO_3 planes along the nearly closed packed (eutactic) direction, which are also known as polytypes [18,19]. Due to the large cationic radii of Sr and Ba (compared to Ca, which is orthorhombic in the ground state) [23], these manganite perovskites are stable as hexagonal structures, as predicted from the Goldschmidt tolerance factor ($t > 1$) [24]. For ground state hexagonal structures, two main stacking sequences are of interest for this paper: $ABAC$, or the $4H$ structure, and $ABAB$, or the $2H$ structure. The metastable cubic structure has a stacking sequence of ABC and is also known as the $3C$ structure. $4H$ $SrMnO_3$ ($t \approx 1.033$) [12] is stable in bulk at low temperatures, but can be transformed to the metastable $3C$ structure at high temperatures around 1400 °C [18]. $BaMnO_3$ ($t \approx 1.097$) [12] is stable in bulk in the $2H$ structure, and the high temperature (around 1550 °C) structure is $4H$ [19]. The existence of these polytypes for (Sr/Ba)MnO_3 materials leads to the question of how to alter phase stability using epitaxy. In other words, how does epitaxy alter the nucleation energetics of the different phases, as determined by DFT?

Oxygen vacancies in (Sr/Ba)MnO_3 materials are thought to play important roles in stabilization of metastable cubic stacking phases that have lower tolerance factors. This stabilization is typically explained using the charge compensation of oxide vacancies with 2 Mn^{3+} cations (replacing 2 smaller Mn^{4+} cations), which leads to a larger average ionic radii for Mn and decreases the tolerance factor and stabilizes cubic stacking [18,25]. Experimentally, increased oxygen vacancy concentrations can be achieved using higher substrate temperatures, lower oxygen partial pressures, and strain [12,20,21,25,26]. One might expect that DFT can capture phase stability versus non-stoichiometry in such systems, assuming the ground state stability varies with composition. While it is common to compute the oxygen vacancy formation energy as a function of strain using DFT (usually in $3C$ polytypes) [12,27,28], it is less common to explore phase stability with DFT while also considering non-stoichiometry. As we want CGES to be accessible to the experimentalist, we briefly explore non-stoichiometry using standard DFT methods (in the Supplemental Information) and show that stoichiometric $SrMnO_3$ cells are sufficient to predict polymorph stability trends on differently oriented $SrTiO_3$ substrates (largely because the bulk internal energies are not significantly shifted).

Many computational and experimental studies focus on the properties of the $3C$ structure of (Sr/Ba)MnO_3 due to interesting multiferroic properties [11,12,29–35]. $SrMnO_3$ and $BaMnO_3$ are G-type antiferromagnetic (AFM) and paraelectric in their ground states, but strain and oxygen vacancies are key parameters that alter their magnetic and electric properties [12,27,28,36,37]. First-principles calculations have shown that, for $SrMnO_3$, a large enough tensile strain can lead to a ferroelectric (FE) ferromagnetic (FM) phase [38]. Experimentally, $SrMnO_3$ has been shown to be ferroelectric as a film when strained to >1% [31,35]. For $BaMnO_3$, the cubic perovskite structure has never been formed experimentally but has been predicted by DFT to be ferroelectric with a polarization of 12.8 μC/cm^2 with AFM ordering due to the off-centering of the magnetic Mn^{4+} ion [11]. Further, a FE-FM phase has been predicted for strained and unstrained $3C$ $BaMnO_3$ [12,39].

While computations can guide experimentalists towards interesting properties in metastable materials, there are no robust computational predictive tools for synthesis. The main purpose of this study is to analyze the computed energetics of (Sr/Ba)MnO_3 polymorph competition and compare how they relate to experimental results, to guide thin film experiments in realizing a $3C$ $BaMnO_3$ film. Additionally, We briefly discuss our results in the context of the 20 kJ/mol epitaxial stabilization limit proposed by Mehta et al. [14]

2. Computational methods

DFT calculations were carried out using the plane-wave self-consistent field (PWscf) package of the Quantum ESPRESSO (QE) distribution [40]. Projector augmented wave (PAW) pseudopotentials are used for the exchange–correlation potential in the Perdew–Burke–Ernzerhof (PBE) parameterization [41–43]. The kinetic energy cut-off was 80 Ry for all structures. Since CGES is used as a predictive tool for synthesis at elevated temperatures (ranging around 950–1150 K), all calculations are non-spin polarized as magnetic ordering for these materials are predicted to exist at temperatures lower than 300 K [44].

The model used by Xu et al. [15] to calculate the energetic difference between the nucleation of two competing epitaxial phases is derived from continuum level capillarity theory [15,45,46]. The equation for the energetic difference, ΔE, between the metastable phase (II) and stable phase (I) is shown in Eq. (1):

$$\Delta E^{II-I} = [(\Delta E_b^{II} + \Delta E_w^{II}) - (\Delta E_b^{I} + \Delta E_w^{I})]d + (\sigma_{int}^{S\|II} - \sigma_{int}^{S\|I}) \quad (1)$$

where ΔE_b is the bulk formation energy, ΔE_w is the bulk strain energy, d is the film thickness, and σ_{int} is the film–substrate (S) interface energy. d is set at 1 nm as an upper limit to the nucleation of thin film layers [15]. This equation neglects the term for the surface energy, or σ_{surf}, because of difficulties in accurately determining the lowest energy surface reconstruction, especially for polar surfaces [47–49]. Therefore, similarly to Xu et al. [15] we assume that the differences in surface energies between the metastable and stable phase are negligible.

Based on Eq. (1), three types of structures were constructed for the energetic calculation of epitaxial phase stability: (relaxed) bulk, strained (bulk), and interface structures. For cubic and hexagonal formation and strain energy calculations, k-points were represented on Γ-centered 10 × 10 × 10 and 9 × 9 × 1 Monkhorst–Pack grids, respectively. These parameters were determined by testing convergence in self-consistent calculations. For interface calculations, determination of an appropriate k-point density is more time-consuming and difficult because of the larger number of atoms required. Convergence parameters were determined for the $(100)[010]_{3C,\ SrMnO_3} \parallel (100)[010]_{3C,\ SrTiO_3}$ interface and then applied to the other interface energy calculations. More information on the construction of the strained and interface cells can be found in the Supplemental Information (SI), Section S1.

Bulk formation energies are calculated using one unit cell for each structure. For $3C$ structures, one unit cell contains 5 atoms, which is equivalent to one formula unit of (Sr/Ba)MnO_3. For $2H$ and $4H$ structures, there are 10 and 20 atoms, respectively, which is equivalent to 2 and 4 formula units. The formation energy per formula unit is calculated by subtracting the energy of the ternary compound by the energy of its binary oxide compounds:

$$\Delta E_b = E_{(Sr/Ba)MnO_3} - E_{MnO_2} - E_{(Sr/Ba)O} \quad (2)$$

where E_{MnO_2} and $E_{(Sr/Ba)O}$ are the energies per formula unit of MnO_2 and (Sr/Ba)O, respectively. Binary oxides are used in the calculation of bulk formation energies in Eq. (2) because they are chemically more similar to the ternary oxides compared to the individual elements. This has been shown to be more accurate in computing the formation energies and phase stabilities of ternary oxides [50].

The strain energies were computed by straining the in-plane lattice parameters of (Sr/Ba)MnO_3 to that of the (Sr/Ba)TiO_3 substrate, using the experimentally determined ORs. For each substrate, three orientations were constructed – the (100), (110), and (111) – by using a transformation matrix such that the (hkl) surface normal was parallel to the z-axis and the periodicity was retained. More information on the construction of each orientation, as well as depictions of each cell, can be found in Section S1. For $3C$ film structures on (Sr/Ba)TiO_3, the alignment is simply cube-on-cube. $3C$ film structures were transformed to their respective substrate orientations and strained in the x and y directions. For $2H$ and $4H$ film structures, the film is only coherent on (Sr/Ba)TiO_3 (111) substrates, with a film orientation of (001). The hexagonal (001)-oriented film structures were transformed to orthorhombic structures with the same orientation, and strained in-plane to the substrate lattice parameters. A table of the specific ORs used

Table 1
Specific orientation relationships between (Sr/Ba)MnO_3 polytypes and (Sr/Ba)TiO_3 used for computations of interface energy values). S indicates the substrate, and f indicates the film. In the last four columns, the values on the left of the slash are for $SrMnO_3$, and values on the right are for $BaMnO_3$. – indicates no computation.

Polytype	Interface	In-plane alignment	Vector strain (%)		Area strain (%)	
	$(hkl)_S \parallel (hkl)_f$	$[uvw]_S \parallel [uvw]_f$	STO	BTO	STO	BTO
3C	(100)‖(100)	[010]‖[010] [001]‖[001]	+3.68/+0.77 +3.68/+0.77	–/+3.07 –/+3.07	+7.50/+1.54	–/+6.23
	(110)‖(110)	[$\bar{1}$10]‖[$\bar{1}$10] [00$\bar{1}$]‖[00$\bar{1}$]	+3.53/+0.72 +3.68/+0.77	–/+3.07 –/+3.07	+7.35/+1.50	–/+6.24
	(111)‖(111)	[$\bar{1}$10]‖[$\bar{1}$10] [$\bar{1}\bar{1}$2]‖[$\bar{1}\bar{1}$2]	+3.53/+0.72 +3.65/+0.84	–/+3.07 –/+3.13	+7.31/+1.57	–/+6.31
4H	(111)‖(001)	[$\bar{1}$10]‖[100] [$\bar{1}\bar{1}$2]‖[120]	+2.37/−1.07 +2.37/−1.03	–/+1.24 –/+1.23	+4.80/−2.08	*/+2.49
2H	(111)‖(001)	[$\bar{1}$10]‖[100] [$\bar{1}\bar{1}$2]‖[120]	–/−2.62 –/−2.62	–/−0.35 –/−0.40	–/−5.18	–/−0.75

in this paper are shown in Table 1. Additionally, the strain of each in-plane vector, as well as the area strain, are calculated in Table 1. In the last four columns, the values on the left of the slash are for $SrMnO_3$, and values on the right are for $BaMnO_3$. Only $BaMnO_3$ was computed on $BaTiO_3$ substrates, and $SrMnO_3$ was not computed in the 2H structure. All ORs are consistent with general eutactic OR arguments. For each substrate plane, the two orthogonal in-plane directions are listed as reference. For all strained film structures, optimized atomic positions were found by relaxing the atoms along the z-axis. Finally, the strain energy contribution, ΔE_w, is calculated by subtracting the bulk energy, E_b, from the total energy of the strained cell, E_{b+w}:

$$\Delta E_w = E_{b+w} - E_b \tag{3}$$

For the incoherent hexagonal (Sr/Ba)MnO_3 orientations on (100) and (110) (Sr/Ba)TiO_3 substrates, the strain energy is assumed to be 0 kJ/mol.

Interface energies were computed by stacking the (Sr/Ba)MnO_3 structures on (Sr/Ba)TiO_3 structures along the z-axis according to the ORs shown in Table 1. The cells are stoichiometric but non-symmetric with respect to the z-axis. An example interface cell for the 4H $BaMnO_3$ (001) interface with 3C $SrTiO_3$ (111) is shown in Fig. 1. The interface plane is perpendicular to the z-axis. In this construction, there are 3 layers (6 unit cells) of $SrTiO_3$ and 4 layers (8 unit cells) of 4H $BaMnO_3$ stacked along the z-axis (within the overall interfacial cell), and there are two interfaces (one at $z = 0$ and one at $z \approx \frac{3}{7}$). The blue TiO_6 and purple MnO_6 octahedra share corners at the interface. More detailed comparisons between 3C, 4H, and 2H stacking sequences and repeating interface cells are given in Section S2, Figure S2. For 3C (111) interfaces, there are 6 layers (12 unit cells) of each phase, and two interfaces (one at $z = 0$ and one at $z \approx \frac{6}{12}$). For the 2H $BaMnO_3$ (001) interface construction with 3C (Sr/Ba)TiO_3 (111), the 3C substrate and 4H film layers (unit cells) alternate in a pattern of 3-4-3-4 (6-8-6-8), respectively, leading to 4 interfaces (z = 0 and $\approx \frac{3}{14}$, $\frac{7}{14}$, and $\frac{10}{14}$) in an interfacial cell; this construction retained complete corner-sharing of octahedra at the interface. While the basic atomic arrangements are nominally the same between 4H and 2H interfaces, e.g. corner sharing octahedra, the Ti–O and Mn–O bond lengths and the Ti–O–Mn angles will be different owing to the specific relaxation method used for the computation of ΔE_{b+w}, which only allows atoms to relax in the z-direction. Variations in bond lengths and angles result in different interface energies between 2H and 4H films on (111) substrates. Face-sharing constructions were also computed but are not reported because all constructions with corner-sharing octahedra at the interface had lower interface energies compared to those with face-sharing interfaces.

The interface energy for (Sr/Ba)MnO_3 and the 3C (Sr/Ba)TiO_3 substrates are calculated using the following equation:

$$\sigma_{int}^{S\parallel f} = \frac{1}{2A}(E_b^{S\parallel f} - nE_b^S - mE_{b+w}^f) \tag{4}$$

where $\sigma_{int}^{S\parallel f}$ is the interface energy between the substrate (S) and film (f), A is the area of the interface plane, E_b^S is the bulk energy of the substrate, and E_{b+w}^f is the strained bulk energy of the film. n and m are the number of unit cells in the interface construction. For 2H $BaMnO_3$ interface constructions on (111) (Sr/Ba)TiO_3 substrates, there are 4 interfaces, so the value of 2 in the denominator is replaced by 4. For incoherent hexagonal structures on (100) and (110) (Sr/Ba)TiO_3 substrates, the interface energy is assumed to be 1 J/m^2 [3,15].

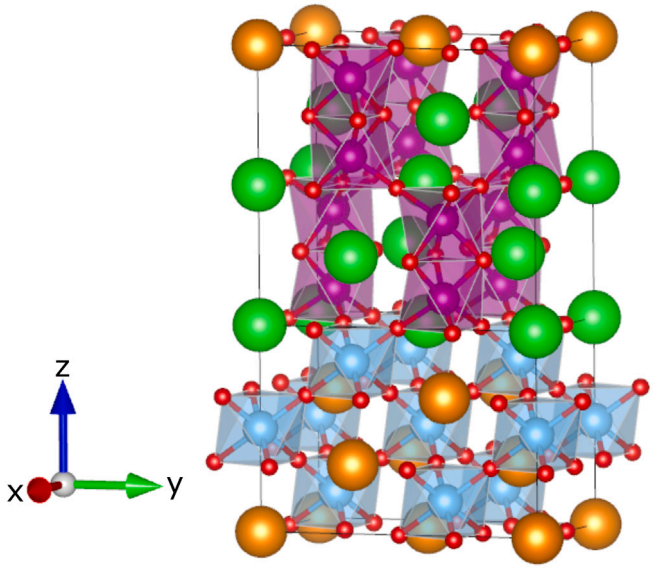

Fig. 1. Example of a coherent interface cell. The unit cell on top is the (001) 4H $BaMnO_3$ on (111) $SrTiO_3$ (bottom). Sr is represented by orange circles, Ba by green circles, and O by red circles. Ti and Mn are represented by blue and purple circles, respectively, located at the centers of their similarly colored octahedra.

3. Results

The equilibrium bulk formation energy and strain energy for the $SrMnO_3$ and $BaMnO_3$ polytypes on (Sr/Ba)TiO_3 are shown in Tables 2 and 3, respectively. The difference in formation energy between the 3C and 4H $SrMnO_3$ is 25.56 kJ/mol. This is consistent with previous DFT calculations, even where magnetic ordering is considered [29,51]. The difference in formation energy between 3C and 4H $BaMnO_3$ is 61.25 kJ/mol in favor of the 4H phase; between 4H and 2H $BaMnO_3$, the difference in formation energy is 24.66 kJ/mol in favor of the 2H phase. These relative formation energy values for $BaMnO_3$ are again consistent with previous DFT calculations [29]. The bulk formation energies for $SrMnO_3$ and $BaMnO_3$ are consistent with the experimentally observed phase stability [18,19].

The bulk strain energy contributions, ΔE_w, are by definition positive and, as expected, smaller in magnitude than the bulk formation

Table 2
Formation energies of $SrMnO_3$ polytypes and their epitaxial strain energies on $SrTiO_3$ substrates with specified interfaces.

$SrMnO_3$ polytype	ΔE_b (kJ/mol)	Interface ($S \parallel f$)	ΔE_w (kJ/mol)	ΔE_{b+w} (kJ/mol)
3*C*	−50.73	(100) ‖ (100)	8.54	−42.19
		(110) ‖ (110)	12.79	−37.94
		(111) ‖ (111)	14.42	−36.31
4*H*	−76.29	(111) ‖ (001)	7.33	−68.96

Table 3
Formation energies of $BaMnO_3$ polytypes and their epitaxial strain energies on (Sr/Ba)TiO_3 substrates with specified interfaces.

$BaMnO_3$ polytype	ΔE_b (kJ/mol)	Interface ($S \parallel f$)	ΔE_w (kJ/mol)		ΔE_{b+w} (kJ/mol)	
			STO	BTO	STO	BTO
3*C*	−40.82	(100) ‖ (100)	0.51	5.60	−40.31	−35.22
		(110) ‖ (110)	1.16	10.98	−39.66	−29.84
		(111) ‖ (111)	2.59	12.99	−38.23	−27.83
4*H*	−102.07	(111) ‖ (001)	3.89	3.86	−98.40	−98.18
2*H*	−126.73	(111) ‖ (001)	7.02	2.60	−119.71	−124.13

energies. For a given substrate orientation, we observe that a higher area strain (see Table 1) leads to a higher value of ΔE_w, in agreement with the observations of Xu et al. [15]. For example on (100) $SrTiO_3$, the strain is larger in-plane for (100) 3*C* $SrMnO_3$ than it is for (100) 3*C* $BaMnO_3$ (+7.50% vs. +1.54%), and this is reflected in the strain energy (8.54 kJ/mol vs. 0.51 kJ/mol). When comparing 3*C* $SrMnO_3$ on $SrTiO_3$ with 3*C* $BaMnO_3$ on $BaTiO_3$, for a given orientation, the area strains are quite similar, resulting in similar strain energy contributions as well. However, area strains are not good predictors for strain energies of 3*C* polytypes on a given substrate as a function of orientation. For all 3*C* polytypes, the strain energy penalty is smallest on the (100) oriented 3*C* substrate, followed by the (110) and then the (111), even though the area strains do not vary greatly. Surprisingly, the strain energy penalties for 3*C* $BaMnO_3$ on (111)-oriented substrates are more than double than those on (100)-oriented substrates. The large differences as a function of orientation are correlated with differences in unit cell volume and volumetric strains (see Tables S1-S6 in Section S3). In other words, the strain energies are correlated to the volumetric strain. More discussion on the possible mechanisms behind the increase in strain energy can be found in the next section.

On (111) substrate orientations, the strain energy contribution was computed for hexagonal polytypes, so comparisons with the 3C polytype can be made. For $SrMnO_3$ on (111) $SrTiO_3$, the 4*H* polytype only has a strain energy penalty of 7.33 kJ/mol, which is significantly lower than that of the 3*C* polytype (14.42 kJ/mol). The percent difference in area strain between the two polytypes follows the same trend in that the 4*H* has a lower strain per area, +4.78%, compared to the 3*C* phase, +7.31%. For $BaMnO_3$ on (111) $SrTiO_3$, the strain energy penalty is lowest for the 3*C* polytype, 2.59 kJ/mol, and highest for the 2*H* polytype, 7.02 kJ/mol. The 3*C* polytype experiences a small tensile strain in the plane whereas the hexagonal polytypes are compressed in-plane. The magnitude of their respective percent change in area strain in Table 1 increases from 3*C* to 4*H* to 2*H*, following the trend with increasing strain energy. For $BaMnO_3$ on (111) $BaTiO_3$, the strain energy is highest for the 3*C* polytype (12.99 kJ/mol) and lowest for the 2*H* polytype (2.60 kJ/mol). Likewise for the strain area, the magnitude of the area strain is highest for the 3*C* polytype (+6.31%) and lowest (−0.75%) on the 2*H* polytype.

Tables 4 and 5 show the computed interface energy values of $SrMnO_3$ and $BaMnO_3$ polytypes on different (Sr/Ba)TiO_3 substrate orientations, respectively. For all 3*C* polytypes, the interface energy with (Sr/Ba)TiO_3 substrates is quite low for all three substrate orientations considered, having a maximal value of 0.066 J/m^2. This is not surprising since the film and substrate are isostructural. These results are consistent with the expected range of a coherent epitaxial interface [3]. Generally, the (100) interface has the highest energy for

Table 4
Interface energies of $SrMnO_3$ polytypes on $SrTiO_3$ substrate orientations.

$SrMnO_3$ polytype	Interface ($S \parallel f$)	σ_{int} (J/m^2)
3*C*	(100) ‖ (100)	0.039
	(110) ‖ (110)	0.066
	(111) ‖ (111)	0.009
4*H*	(111) ‖ (001)	0.128

Table 5
Interface energy of $BaMnO_3$ polytypes on (Sr/Ba)TiO_3 substrate orientations.

$BaMnO_3$ polytype	Interface ($S \parallel f$)	σ_{int} (J/m^2)	
		STO	BTO
3*C*	(100) ‖ (100)	0.034	0.024
	(110) ‖ (110)	0.004	0.006
	(111) ‖ (111)	0.005	1.35×10^{-4}
4*H*	(111) ‖ (001)	0.185	0.103
2*H*	(111) ‖ (001)	0.193	0.241

all 3*C* interfaces (between 0.024 and 0.039 J/m^2), while the (111) interface has the lowest energy (between 0.0001 and 0.009 J/m^2). The (110) 3*C* $BaMnO_3$ interfaces are also low (0.004–0.006 J/m^2), while (110) 3*C* $SrMnO_3$ interface with (110) $SrTiO_3$ is even higher than (100) at 0.066 J/m^2.

For all coherent interfaces involving hexagonal film structures on (111) cubic substrates, the interface energy penalty is greatly lowered compared to the assumed value for incoherent interfaces on (100) and (110) substrates (1 J/cm^2). For (001) 4*H* $SrMnO_3$ on (111) $SrTiO_3$, the interface energy is 0.128 J/m^2, which is significantly larger compared to the 3*C* phase on the same substrate and orientation (0.009 J/m^2). For $BaMnO_3$ on (111) (Sr/Ba)TiO_3, the 2*H* polytype has the largest interface energy per unit area compared to the 4*H* and 3*C* phases. These 2*H* interface energies are 0.193 and 0.241 J/m^2, on $SrTiO_3$ and $BaTiO_3$, respectively. The interface energy values of 4*H* $BaMnO_3$ polytype on the (111) substrates are lower, at 0.185 and 0.103 J/m^2 on $SrTiO_3$ and $BaTiO_3$, respectively. The interfacial energies of the 3*C* $BaMnO_3$ polytype are 0.005 and near 0 J/m^2 on $SrTiO_3$ and $BaTiO_3$ (111), respectively. In general, interfacial energy contributions to epitaxial stabilization favor the cube-on-cube epitaxial relationship (i.e. the 3*C* polytype) over the hexagonal polytypes.

Table 6 shows the thermodynamic terms used for the calculation of ΔE^{3C-4H} in Eq. (1) for $SrMnO_3$ polytypes on $SrTiO_3$. Column 1 shows the substrate orientation. Columns 2 and 3 show the results of the volumetric formation and volumetric strain energy contributions per unit area for 3*C* and 4*H* phases, respectively. $\Delta E_{b+w}^{4H-SMO}d$ for (100)

Table 6
Thermodynamic terms relevant to epitaxial nucleation of $SrMnO_3$ polytypes on $SrTiO_3$ (J/m^2).

$(hkl)_{STO}$	$\Delta E_{b+w}^{3C-SMO}d$	$\Delta E_{b+w}^{4H-SMO}d$	$\Delta\Delta E_{b+w}^{3C-4H}d$	$\Delta\sigma_{int}^{3C-4H}$	ΔE^{3C-4H}
(100)	−1.285	−2.182*	0.897*	−0.961*	−0.064*
(110)	−1.167	−2.182*	1.015*	−0.934*	0.081*
(111)	−1.122	−1.980	0.858	−0.119	0.739

ΔE^{3C-4H} is computed with $d = 1$ nm.
*Asterisks indicate values that were estimated due to incoherent interfaces; the strain was approximated as 0 kJ/mol and the interface was set at 1 J/m^2.

Table 7
Thermodynamic terms relevant to epitaxial nucleation of $BaMnO_3$ polytypes on $SrTiO_3$ (J/m^2).

$(hkl)_{STO}$	$\Delta E_{b+w}^{3C-BMO}d$	$\Delta E_{b+w}^{4H-BMO}d$	$\Delta\Delta E_{b+w}^{3C-4H}d$	$\Delta\sigma_{int}^{3C-4H}$	ΔE^{3C-4H}
(100)	−1.120	−2.682*	1.562*	−0.966*	0.596*
(110)	−1.102	−2.682*	1.580*	−0.996*	0.584*
(111)	−1.063	−2.584	1.521	−0.180	1.341
$(hkl)_{STO}$	$\Delta E_{b+w}^{4H-BMO}d$	$\Delta E_{b+w}^{2H-BMO}d$	$\Delta\Delta E_{b+w}^{4H-2H}d$	$\Delta\sigma_{int}^{4H-2H}$	ΔE^{4H-2H}
(100)	−2.682*	−3.101*	0.419*	0*	0.419*
(110)	−2.682*	−3.101*	0.419*	0*	0.419*
(111)	−2.584	−2.921	0.337	−0.008	0.329

ΔE^{3C-4H} and ΔE^{4H-2H} are computed with $d = 1$ nm.
*Asterisks indicate values that were estimated due to incoherent interfaces; the strain was approximated as 0 kJ/mol and the interface was set at 1 J/m^2.

Table 8
Thermodynamic terms relevant to epitaxial nucleation of $BaMnO_3$ polytypes on $BaTiO_3$ (J/m^2).

$(hkl)_{BTO}$	$\Delta E_{b+w}^{3C-BMO}d$	$\Delta E_{b+w}^{4H-BMO}d$	$\Delta\Delta E_{b+w}^{3C-4H}d$	$\Delta\sigma_{int}^{3C-4H}$	ΔE^{3C-4H}
(100)	−0.982	−2.682*	1.700*	−0.976*	0.724*
(110)	−0.841	−2.682*	1.842*	−0.994*	0.848*
(111)	−0.789	−2.582	1.793	−0.103	1.690
$(hkl)_{BTO}$	$\Delta E_{b+w}^{4H-BMO}d$	$\Delta E_{b+w}^{2H-BMO}d$	$\Delta\Delta E_{b+w}^{4H-2H}d$	$\Delta\sigma_{int}^{4H-2H}$	ΔE^{4H-2H}
(100)	−2.682*	−3.101*	0.419*	0*	0.419*
(110)	−2.682*	−3.101*	0.419*	0*	0.419*
(111)	−2.582	−3.037	0.455	−0.138	0.317

ΔE^{3C-4H} and ΔE^{4H-2H} are computed with $d = 1$ nm.
*Asterisks indicate values that were estimated due to incoherent interfaces; the strain was approximated as 0 kJ/mol and the interface was set at 1 J/m^2.

and (110) substrate orientations are estimated due to the incoherent interface with the $4H$ phase; only the volumetric formation energy is considered because there is no strain energy contribution. Column 4 is the volumetric energy difference between polytypes, $\Delta\Delta E_{b+w}^{3C-4H}d$, and is calculated by subtracting the second column by the third. The value of $\Delta\Delta E_{b+w}^{3C-4H}d$ is highest on (110) $SrTiO_3$ (1.015 J/m^2) and lowest on (111) $SrTiO_3$ (0.858 J/m^2). Column 5 is the difference in interface energies between the $3C$ and $4H$ phases from Table 4. The high incoherent interface energy value contributes significantly to favor the $3C$ phase on (100) and (110) substrate orientations. The energetic contributions of $\Delta\Delta E_{b+w}^{3C-4H}d$ and $\Delta\sigma_{int}^{3C-4H}$ are similar in scale on (100) and (110) $SrTiO_3$, suggesting that interfacial penalties of the $4H$ polytype are as important as the volumetric energy penalties of the $3C$ polytype on these substrate orientations. On (111) $SrTiO_3$, the value of $\Delta\sigma_{int}^{3C-4H}$ is closer to zero (the boundary between $3C$ and $4H$ interface stability), at −0.119 J/m^2, compared to the same values on (100) and (110) $SrTiO_3$. Therefore the volumetric energy terms contribute significantly more than the interface energy to the stabilization of the $4H$ phase on (111) $SrTiO_3$.

Column 6 shows the values for ΔE^{3C-4H}, the total energetic difference between the metastable $3C$ and stable $4H$ polytypes at 1 nm, and is the sum of columns 4 and 5. On (100) $SrTiO_3$, the value of ΔE^{3C-4H} is −0.064 J/m^2, indicating that the $3C$ phase is stable. On (110) $SrTiO_3$, the energetic difference between polytype is 0.081 J/m^2, slightly favoring the $4H$ phase (within the accuracy of the computations). On (111) $SrTiO_3$, the value of ΔE^{3C-4H} is 0.739 J/m^2, indicating that the $4H$ phase is heavily favored as epitaxial stable nuclei. These trends in ΔE^{3C-4H} are consistent with experimental results [8,26]. Values from the last three columns of Table 6 are plotted in Fig. 2(a) for $SrMnO_3$ on $SrTiO_3$ substrates.

Tables 7 and 8 show the thermodynamic terms used for the calculation of Eq. (1) for $BaMnO_3$ polytypes on $SrTiO_3$ and $BaTiO_3$, respectively. These tables are organized similarly to Table 6, with the addition of $2H$ $BaMnO_3$ energetic terms at 1 nm. The ΔE values are calculated for the difference between $3C$ and $4H$ polytypes, as well as between $4H$ and $2H$ polytypes. Values for the energetic differences between $3C$ and $4H$ phases from the last three columns of Tables 7 and 8 are plotted in Figs. 2(b) and (c), respectively. The energetic differences between $3C$ and $2H$ polytypes can simply be calculated by adding ΔE^{3C-4H} and ΔE^{4H-2H}. For incoherent hexagonal polytypes on (100) and (110) substrates, only differences in volumetric formation energy are calculated. In reality, there may be energetic differences for the incoherent hexagonal films on these two substrates. None of the final ΔE values are negative, indicating that under DFT 0 K conditions, the $3C$ polytype for $BaMnO_3$ is never more stable than the hexagonal polytypes.

When considering the polymorph competition between $4H$ and $3C$ $BaMnO_3$, the lowest energetic difference (or ΔE^{3C-4H}) is on (110) $SrTiO_3$. On this substrate and orientation, ΔE^{3C-4H} is 0.584 J/m^2. On (100) $SrTiO_3$, the value of ΔE^{3C-4H} is 0.596 J/m^2, which is only 0.012 J/m^2 higher than the same polytype competition on (110) $SrTiO_3$. While the energetic difference between polytypes is similar on (100) and (110) $SrTiO_3$ substrate orientations, the ΔE^{3C-4H} value is much higher on $SrTiO_3$ (111), at 1.341 J/m^2. Between hexagonal polytypes however, the energetic difference between $2H$ and $4H$ polytypes is only 0.329 J/m^2, in favor of the $2H$ on (111) $SrTiO_3$. While this is the smallest value of energy considering the $4H$ $BaMnO_3$ phase versus the $2H$ one, it is still considerably larger than the ΔE^{3C-4H} values stabilizing 3C $SrMnO_3$ on (100) and (110) $SrTiO_3$. Moreover, all $BaMnO_3$ orientations required more energy compared to $SrMnO_3$ to transform the $4H$ phase to the $3C$ (summing appropriate entries in the last column), and the order of stability is (110)<(100)<(111) on $SrTiO_3$.

For the $BaMnO_3$ polytypes on $BaTiO_3$ in Table 8, thermodynamic terms are generally higher in energy compared to films on $SrTiO_3$. The volumetric energy values for $3C$ $BaMnO_3$, $\Delta E_{b+w}^{3C-BMO}d$, are all larger on $BaTiO_3$ than on $SrTiO_3$ due to larger strain energies. For ΔE^{3C-4H}, the lowest energetic competition between $3C$ and $4H$ $BaMnO_3$ polytypes is on (100) $BaTiO_3$, at 0.724 J/m^2. On (111) $BaTiO_3$, ΔE^{3C-4H} is much larger, at 1.690 J/m^2. However, the ΔE^{4H-2H} on (111) $BaTiO_3$ is only 0.317 J/m^2. This value is 0.012 J/m^2 less than ΔE^{4H-2H} for $BaMnO_3$ on (111) $SrTiO_3$, indicating that stabilization of the $4H$ phase is slightly more favorable on (111) $BaTiO_3$.

Fig. 3 shows the plots of ΔE^{3C-4H} as a function of the number (or thickness) of $3C$ film layers for each film/substrate combination. The thickness of one $3C$ layer is defined as the distance between planes (more widely known as the d-spacing) that bound one electroneutral stoichiometric layer. The layer thicknesses for $3C$ $SrMnO_3$ (100), (110), and (111) are 0.380, 0.269, and 0.220 nm, respectively. For $3C$ $BaMnO_3$, they are 0.391, 0.276, and 0.226 nm, respectively. For every film/substrate combination, the $3C$ film phase is stable ($\Delta E^{3C-4H} <$ 0 J/m^2) on (100) and (110) substrate orientations at a nucleation thickness of 1 layer. The values for ΔE^{3C-4H} on (111) substrate orientations are always positive, indicating that the $3C$ will never be stable in that orientation. The results in Fig. 3 show how nucleation thickness modifies the competition between volumetric energy terms and interface energy terms, which can lead to the stabilization of very metastable phases at low thickness values, including $3C$ $BaMnO_3$.

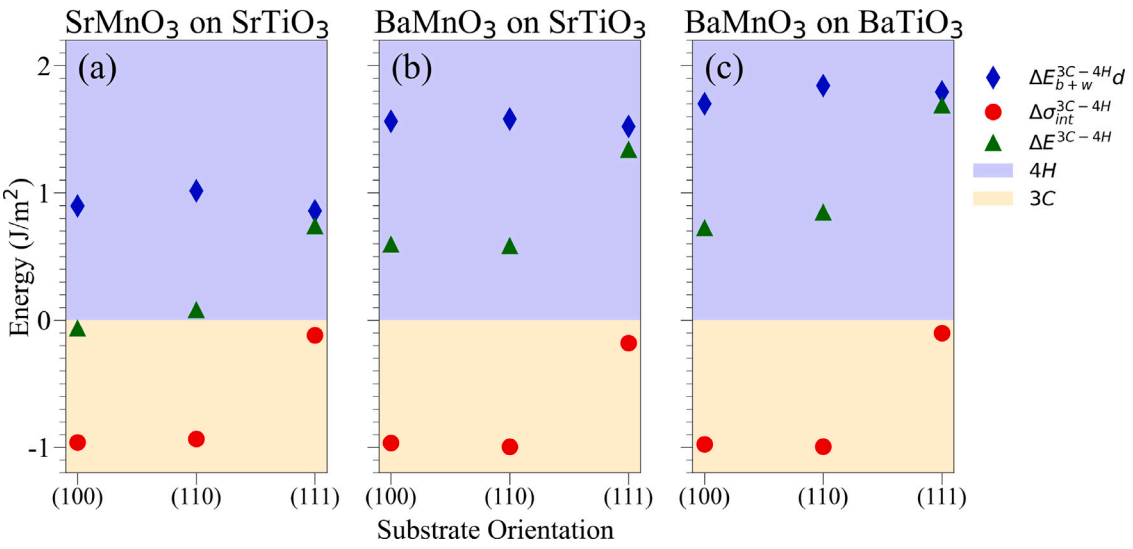

Fig. 2. Plots of the energetic differences between $3C$ and $4H$ polymorphs for each film/substrate combination. The x-axes indicate the substrate orientations. Blue diamonds, red circles, and green triangles indicate the values for $\Delta E_{b+w}^{3C-4H}d$, $\Delta\sigma_{int}^{3C-4H}$, and ΔE^{3C-4H}, respectively. These values are also presented in the last three columns from Tables 6, 7, and 8, for (a), (b), and (c), respectively. Blue and orange background colors indicate the range of energies where the $4H$ and $3C$ are stable, respectively, for the ΔE^{3C-4H} values in green triangles.

4. Discussion

Using standard DFT methods to quantify energetic terms in a typical model for nucleation, we computed the relative stability of epitaxial polytypes of (Sr/Ba)MnO_3 on (Sr/Ba)TiO_3 substrates of three low-index orientations. We call this approach CGES, because such computations are useful in guiding epitaxial stabilization of metastable phases, as they offer insight into which substrates and orientations are most stabilizing. Here we discuss the strengths and limitations of CGES as currently implemented.

For the case of $SrMnO_3$ on $SrTiO_3$, we can compare the DFT results to experimental work [7,8,26]. The CGES results described herein indicate that the stability for the metastable $3C$ $SrMnO_3$ phase decreases at a given thickness from (100) to (110) to (111) $SrTiO_3$. This is consistent with experimental work [7,8] that showed the (100) substrate orientation easily stabilizes the $3C$ phase using typical thin film deposition conditions, the (111) can only stabilize the $3C$ phase at high substrate temperatures and low oxygen pressures [26], and the (110) is intermediate between those others. That the relative order of stability is well matched here, as well as for anatase TiO_2 on (Sr/Ba)TiO_3 [15], indicates that the strength of the CGES model lies in computation of reasonable interface energies.

In the CGES model, the (100) $SrTiO_3$ substrate should always stabilize the $3C$ $SrMnO_3$ (100) phase, at 1 nm thickness. Experimentally, however, this is not entirely borne out. Several studies indicate that both temperature and oxygen pressure mediate the stability of $SrMnO_3$ polymorphs even on (100) $SrTiO_3$ substrates, which is not readily captured by our simple model [7,52–54]. In a study of $SrMnO_3$ on a polycrystalline $SrTiO_3$ substrate by Zhou et al. [7], some $4H$ is observed in a 60 nm $SrMnO_3$ film on a near (100)-oriented substrate grain. While strain leads to the preference for the incoherent $4H$ phase as thickness increases, actual nucleation events depend on the relaxation processes available, which are outside the scope of this simple nucleation model too. Keep in mind that the value of −0.064 J/m^2 for ΔE^{3C-4H} on $SrTiO_3$ (100) is relatively small, so slight deviations in any of the energetic terms or deviations from the modeled nucleation state may lead to changes in net stability. That these experimental film trends follow the known bulk stability likely indicates that the bulk stability terms (E_b and E_{b+w}) vary enough to modify the known stability. Variations in these values, most likely through oxygen vacancies, allow for experimental stabilization of (111) $3C$ $SrMnO_3$ on $SrTiO_3$, herein computed to be less stable by 0.739 J/m^2. To improve CGES, one needs improved computational predictions of bulk stability with temperature and pressure (activity) [55,56].

It is interesting to note the relationship between the in-plane $3C$ strain and strain energy penalty across different substrate orientations, as a small change in the in-plane strain appears to result in a large energy penalty. Tables S1, S3, and S5 show that the change in the unit cell volume, or the volumetric strain given in Tables S2, S4, and S6, is a better predictor of the increase in strain energy for each orientation. Figure S3 compares the volumetric energy (ΔE_{b+w}) of cubic $SrMnO_3$ unit cells of different volumes (whose atom positions are allowed to fully relax) to the same for epitaxially strained $SrMnO_3$ on $SrTiO_3$ (whose atom positions are only allowed to relax in the out-of-plane (c-axis) direction). The results are consistent with typical energy minimization methods, where the relationship between formula unit volume and formation energy is approximately parabolic [12]. The minimum energy corresponds to the fully relaxed unit cell with no strain applied. Formation energies are slightly higher for the epitaxially strained unit cells compared to the cubic strained values, owing to the constraints of relaxing atom positions in only one direction instead of three and changing symmetry owing to the Poisson effect in the epitaxial cases. In the cubic (fully relaxed) cases, the Mn–O bond length varies while the inter-octahedra Mn–O–Mn (cis intra-octahedra O–Mn–O) bond angle remains 180° (90°), and all are single valued. As bi-axial tensile strain is applied by epitaxy, the Poisson effect results in compressive strains out-of-plane (see Tables S1-S6), which leads to non-cubic structures, and up to three distinct values in the Mn–O bond lengths and angles. The O–Mn–O bond angle is found to remain essentially fixed at 180°, indicating the bond lengths and the cis intra-octahedra O–Mn–O accommodate the strain, resulting in a structure whose value is higher in energy than a cubic one of identical volume. The consequence of this preference is that the Poisson effect (and volume change) is a significant function of orientation, with the material becoming significantly stiffer moving from (100) to (110) to (111) epitaxy, under these constraints. Similar trends are found for $BaMnO_3$ on $SrTiO_3$ and $BaTiO_3$.

For $BaMnO_3$, limited experimental work has been reported for thin films [57]. CGES indicates that epitaxial stabilization of the metastable $3C$ films would follow the same trend as $SrMnO_3$. Namely, the (100) perovskite substrate is generally the best orientation on which to stabilize the $3C$ phase and the (111) substrate orientation the worst, with (110) in the middle overall (it is as good as (100) for $SrTiO_3$,

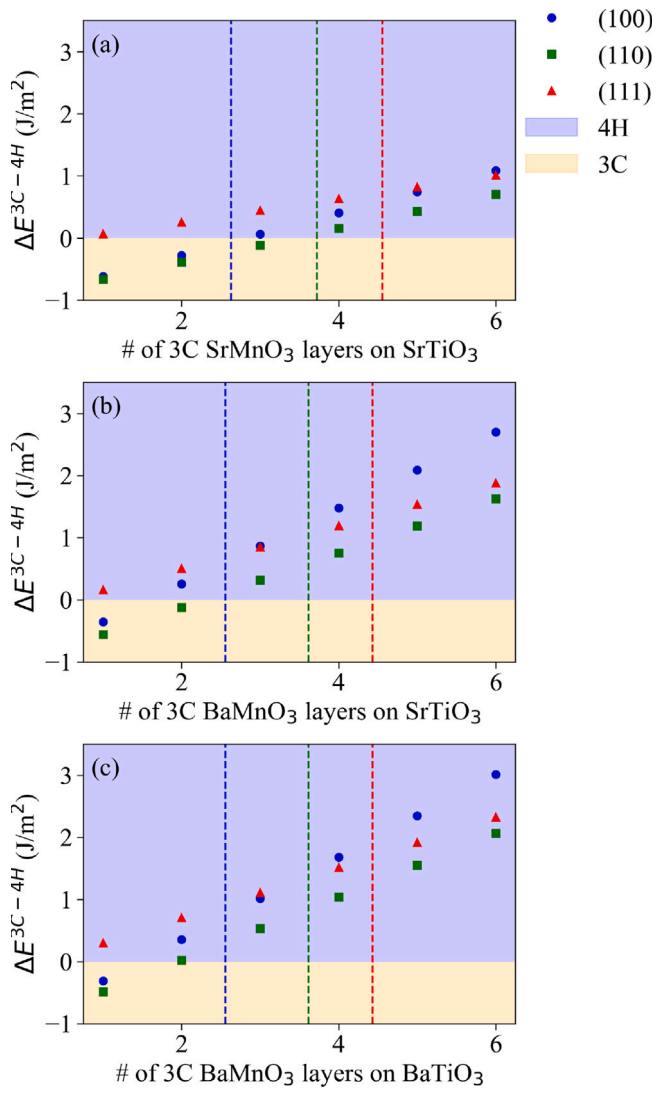

Fig. 3. Plots of ΔE^{3C-4H} as a function of the number of $3C$ layers for each film/substrate combination: (a) $SrMnO_3$ on $SrTiO_3$, (b) $BaMnO_3$ on $SrTiO_3$, and (c) $BaMnO_3$ on $BaTiO_3$. Blue circles, green squares, and red triangles indicate the values of ΔE^{3C-4H} for (100), (110), and (111) substrate orientations, respectively. Vertical lines are colored respectively to their substrate orientations and indicate the number of layers needed for a 1 nm thick film. Blue and orange background colors indicate the range of energies where the $4H$ and $3C$ are stable, respectively.

which is mediated by strain terms). However, the energetic barriers to metastable formation are quite large (> 1 J/m^2 considering $2H$ to $3C$). Considering that we know $SrMnO_3$ experiments have overcome CGES values of 0.739 J/m^2, it may be possible to overcome these barriers with temperature and oxygen pressure. $4H$ $BaMnO_3$ should be more readily achievable on (111) substrates, which are respectively 0.329 and 0.317 J/m^2 on $SrTiO_3$ and $BaTiO_3$. In Section S4, we deposit approximately 150 nm films of $BaMnO_3$ on (111) $SrTiO_3$ substrates using two different deposition pressures: 2×10^{-3} Torr (total pressure achieved using O_2) and 3×10^{-5} Torr (base pressure, no oxygen flow). The X-ray diffraction (XRD) scans show that the film deposited in the higher oxygen pressure environment was $2H$ and that the film deposited in the lower oxygen pressure environment was $4H$. These results indicate that the 0.329 J/m^2 energetic stability for the $2H$ can be overcome using oxygen pressure. Additionally, our results are consistent with stability trends seen in experiments for $SrMnO_3$ on (111) $SrTiO_3$, where higher oxygen pressures do not stabilize the metastable phase [8,26].

The relative stabilities of $4H$ and $2H$ $BaMnO_3$ on (100) and (110) substrates is unknown, as only the volumetric formation energy terms are computed. In reality, there may be differences in the strain and interface energies between the $4H$ and $2H$ polytypes on these substrate orientations that can lead to changes in their ΔE^{4H-2H} values. Therefore the order of stability between hexagonal polytypes may be subject to change from the results presented in Tables 7 and 8. An improved version of CGES would include computed values for the semi-coherent to incoherent interface energies of stable polymorphs on non-isostructural substrates. These values are the phase and crystal structure boundary equivalents of asymmetric grain boundaries, and the latter are becoming more common to be included in computations [58–64]. Owing to the known orientation relationship or epitaxy, only two specific interfaces need to be considered in the more expensive energy computations for incoherent interfaces.

One modification of the relative thermodynamic phase stabilities is through control of the nucleation thickness, as shown in Fig. 3, which controls the volumetric energy terms. Specifically for the competition between $3C$ and hexagonal $BaMnO_3$ films, volumetric energy terms dominate stability at the original value of $d = 1$ nm. When d is limited to a thickness of only 1 layer of (100) or (110) $3C$ $BaMnO_3$ on their respective $SrTiO_3$ and $BaTiO_3$ substrate orientations, the thermodynamic stabilities are reversed and the $3C$ phase is stable. Experimentally, the control of nucleation layer thickness and flatness can be achieved when controlling for thermodynamic and kinetic variables during growth [65].

Since the (Sr/Ba)MnO_3 systems are oxygen deficient, it is well known that an increase in oxygen vacancies can lead to the stabilization of the metastable structures [18,19,25,66,67]. A lower oxygen partial pressure can decrease the temperature at which the stable to metastable transition occurs [20,21]. Zhou et al. [8] reported that the oxygen partial pressure during deposition of a $SrMnO_3$ film on a polycrystalline $SrTiO_3$ substrate affects the range of substrate orientations that can support $3C$ growth. At a substrate temperature of 900 °C, a deposition pressure of 2×10^{-3} Torr pure O_2 does not support $3C$ growth on (111) $SrTiO_3$ but 2×10^{-3} Torr of 1% O_2 ($P_{O_2} = 2\times10^{-5}$ Torr) can, providing evidence that oxygen vacancies can be manipulated instead of (or in addition) to temperature [8].

As discussed above, the phase stability of (Sr/Ba)MnO_3 are a function of temperature and oxygen partial pressure. It is believed that oxygen vacancies impact the bulk formation energy of each phase differently, and can modify overall stability. We calculated the bulk formation energy for two oxygen-deficient $SrMnO_{3-\delta}$ (δ = 0.25 and 0.5), which are shown in Section S5 of the SI. For $3C$ and $4H$ structures, supercells were created in which 1 to 2 oxygen atoms were removed. When comparing the computed energies, the $4H$ structure remained more stable than the $3C$ structure for all compositions, even though the energetic difference becomes slightly smaller for both oxygen-deficient cells (22.94 and 24.54 kJ/mol for δ = 0.25 and 0.5) compared to the stoichiometric one (25.56 kJ/mol). This computation is in agreement with a study by Nielsen et al. [51] on bulk $SrMnO_3$, where they concluded that the transition is actually entropy mediated, which is well outside the scope of this work. The only experimentally available phase transition enthalpy was reported to be 6 ± 2 kJ/mol, for the transition from $3C$ to $4H$ in bulk [66]. This is significantly less than the predicted difference in enthalpies in DFT under 0 K conditions. Furthermore, Søndenå et al. [68] used DFT to compute (and also verified experimentally) the difference in entropy between stoichiometric $SrMnO_3$ polytypes. At 298 K, the entropy difference was 5.6 J/K mol, which gives a phase transition temperature of around 1100 ± 350 K using the experimental phase transition enthalpy. This still does not capture the phase transition temperature of 1673 K, indicating that DFT models do not yet capture the nature of bulk phase stability at high temperatures. It is also implied here that the tolerance factor (bond lengths) for non-stoichiometric materials is not captured so readily without experimental data. In addition to the temperature-dependent oxygen

vacancy concentration, there are also differing thermal expansions between Mn–O and Sr–O bond lengths, which can modify the tolerance factor and enthalpy of the system [69]. Finally, oxygen vacancies can form near the substrate surface prior to film deposition, which can affect the vacancy concentration and stability in the film [70–72]. Therefore CGES can serve as a starting point to guide experimental work, but successful experimental confirmation ultimately relies on combining computations with experimental observations to guide thin film synthesis.

In strongly correlated electron systems, such as in $SrMnO_3$ and $BaMnO_3$, the Hubbard U parameter is often imposed on transition metals for DFT computations (DFT+U) to obtain results that more accurately reflect experimental values [12,28,73,74]. DFT+U improves results by correcting Coulombic interactions between localized d electrons of transition metals [28,74,75]. In Section S6 of the SI, we compute all the thermodynamic terms for Eq. (1) relevant to $3C$ and $4H$ $SrMnO_3$ polytypes on $SrTiO_3$ (111) for a U value of 3 eV [12]. Using this typical U value for Mn, changes in ΔE^{3C-4H} are not significant enough to change the epitaxial stability to favor of the $3C$ phase. The difference in volumetric energy term at 1 nm decreases from 0.858 J/m^2 to 0.775 J/m^2 with the addition of the U parameter, decreasing $4H$ bulk stability. The difference in interface energy moves closer to the phase boundary (0 J/m^2), from −0.119 J/m^2 to −0.099 J/m^2, increasing the penalty for the $3C$ phase. For the strain energy, the U correction penalizes the $3C$ with a higher strain energy on $SrTiO_3$ (111), and decreases it for the $4H$ phase. The total energetic difference for a 1 nm film with competing polymorphs decreases from 0.739 J/m^2 to 0.676 J/m^2. It is difficult to gauge how meaningful this decrease in energetic difference is between polymorphs in terms of experimental conditions. However, incorporating U parameters in CGES studies of other material systems may be more helpful where the bulk energy difference is not as large as that for $SrMnO_3$. Overall, it is clear that most standard DFT methods do not lead to changes in polymorph stability known to occur experimentally. As such, CGES does not capture this either.

Mehta et al. [14] estimated that the epitaxial stability limit was 20 kJ/mol for competing polymorphs, based on similar assumptions for incoherent and coherent films used in this study. This limit was also derived from continuum capillarity theory [45,46] and assumes that, given an ideal substrate, the stable film phase would be incoherent with the substrate, while the metastable film phase would be coherent. In this approximation, however, substrate-film interfaces are idealized and there is no substrate selection. Nonetheless, we can still compare the difference in bulk formation energies of the $SrMnO_3$ to the epitaxial stability limit, to see if the limit is still reasonable as a starting point for epitaxial guidance.

We first test the difference in bulk formation energy between polymorphs in $SrMnO_3$ to see if it is within 20 kJ/mol, and then compare the results to those of $BaMnO_3$. The value of ΔE_b^{3C-4H} is 25.56 kJ/mol, which is slightly higher than the 20 kJ/mol limit and suggests that from a bulk formation energy standpoint, the $3C$ phase would be somewhat difficult to synthesize. By incorporating the specific strain and interface energy of the $SrTiO_3$ substrate and the preferred OR, we see that the $3C$ polytype is predicted to be stable on the (100) substrate. Ultimately, the 25.56 kJ/mol is quite similar to the approximate 20 kJ/mol value (keeping in mind that the experimental value for $SrMnO_3$ was 6 kJ/mol and that non-stoichiometric bulk energy differences are also lower). These values are comparable because they are internally consistent relative to computational terms, and they use the same 1 J/m^2 approximation for the incoherent interface energy term. Of course, the real interface energy term may vary significantly from that value, and we have experimentally observed $3C$ $SrMnO_3$ as epitaxial films [7,8]. Similarly, Lee et al. [76] have been able to stabilize IrO_2 in the metastable columbite structure, which is predicted to be around 25 kJ/mol higher than that of stable rutile IrO_2 [14,76]. These two observations indicate that 25 kJ/mol differences in DFT computed energies are good targets for stability. For $BaMnO_3$, the value of ΔE_b^{4H-2H} is 24.54 kJ/mol, but for ΔE_b^{3C-4H} it is 60.93 kJ/mol. Since ΔE_b^{4H-2H} for $BaMnO_3$ is only 0.89 kJ/mol less than ΔE_b^{3C-4H} for $SrMnO_3$, it could be relatively straightforward to stabilize the $4H$ $BaMnO_3$ via epitaxy, especially on (111) substrate orientations if considering the interface. However, the further transformation from $4H$ to the $3C$ phase may still prove extremely difficult, as the bulk energy requirement is over two times as large as the transformation from $2H$ to $4H$. Even considering substrate orientation, the energetic difference from the ground state $2H$ $BaMnO_3$ phase to the metastable $3C$ phase is quite high, with the lowest value of ΔE^{3C-2H} equal to 1.003 J/m^2 on $SrTiO_3$ (110), which is greater than the incoherent interface energy penalty. Thus, to computationally quantify the potential epitaxial synthesis of $BaMnO_3$, we need a better description of bulk formation energy versus temperature and pressure.

Note that in Eq. (1), the difference in surface energy terms is assumed to be minimal and is thus neglected from these CGES computations. However, their significance should not be totally cast away, as metastable phases have been proposed to form due to lower surface energies [77]. For the case of TiO_2, the difference between anatase and rutile phase stability has sometimes been attributed to differences in surface energies. While rutile is the thermodynamically stable phase, anatase has been observed to be the first phase to form (typically from amorphous precursors) and this has been attributed to its lower surface free energy and subsequent lower barrier to nucleation [78–81]. While it is possible that the inclusion of surface energy terms may significantly change the values of ΔE, the main conclusion from this study is that the order of stability reflects experimental observations without it.

5. Conclusions

Using CGES, we have shown the thermodynamic competition between (Sr/Ba)MnO_3 polytypes on three different (Sr/Ba)TiO_3 substrate orientations. For both $SrMnO_3$ and $BaMnO_3$, the (100) perovskite substrate orientation is the best orientation on which to stabilize the $3C$ phase. The exception to this is (110) $3C$ $BaMnO_3$ on (110) $SrTiO_3$, but only slightly. The (111) substrate orientation is always the least energetically favorable in terms of $3C$ stabilization. We find that (100) $3C$ $SrMnO_3$ on (100) $SrTiO_3$ is the only OR that stabilizes the $3C$ phase at 1 nm, with a negative value of ΔE^{3C-4H}. Our results are consistent with experimental trends for $SrMnO_3$ on $SrTiO_3$ in that the order of substrate orientation to stabilize the $3C$ phase is (100), (110), and then (111). Experimentally, this corresponds to an increase in substrate temperature, or a lower oxygen partial pressure for this system. The agreement with experimental results validates the use of DFT to help guide epitaxy experiments, even though the computational results are for 0 K values—far from experimental conditions. Finally, thermodynamic stabilities can be reversed by limiting the nucleation thickness in order to minimize volumetric energy term contributions, pointing to the possible stabilization of $3C$ $BaMnO_3$ at one or two monolayers (electroneutral layers).

CRediT authorship contribution statement

Catherine Zhou: Conceptualization, Methodology, Software, Validation, Formal analysis, Investigation, Writing – original draft, Visualization. **Gregory S. Rohrer:** Conceptualization, Methodology, Writing – review & editing, Supervision, Project administration, Funding acquisition. **Paul A. Salvador:** Conceptualization, Methodology, Formal analysis, Writing – review & editing, Supervision, Project administration, Funding acquisition.

Declaration of competing interest

The authors declare that they have no known competing financial interests or personal relationships that could have appeared to influence the work reported in this paper.

Data availability

Data will be made available on request.

Acknowledgments

C.Z., P.A.S., and G.S.R. acknowledge the support of the National Science Foundation, United States [DMR-1609355]. This project was also financed in part by a grant from the Commonwealth of Pennsylvania Department of Community and Economic Development. Additionally, the authors thank John R. Kitchin for use of computational resources.

Appendix A. Supplementary data

Supplementary material related to this article can be found online at https://doi.org/10.1016/j.commatsci.2023.112415.

References

[1] P.A. Salvador, T.D. Doan, B. Mercey, B. Raveau, Stabilization of $YMnO_3$ in a Perovskite structure as a thin film, Chem. Mater. 10 (10) (1998) 2592–2595.
[2] B. Mercey, P.A. Salvador, W. Prellier, T.-D. Doan, J. Wolfman, M. Hervieu, B. Raveau, Thin film deposition: A novel synthetic route to new materials, J. Mater. Chem. 9 (1) (1999) 233–242.
[3] O.Y. Gorbenko, S.V. Samoilenkov, I.E. Graboy, A.R. Kaul, Epitaxial stabilization of oxides in thin films, Chem. Mater. 14 (10) (2002) 4026–4043.
[4] D.G. Schlom, L.-Q. Chen, X. Pan, A. Schmehl, M.A. Zurbuchen, A thin film approach to engineering functionality into oxides, J. Am. Ceram. Soc. 91 (8) (2008) 2429–2454.
[5] S. Havelia, S. Wang, K.R. Balasubramaniam, A.M. Schultz, G.S. Rohrer, P.A. Salvador, Combinatorial substrate epitaxy: A new approach to growth of complex metastable compounds, CrystEngComm 15 (2013) 5434–5441.
[6] J. Wittkamper, Z. Xu, B. Kombaiah, F. Ram, M. De Graef, J.R. Kitchin, G.S. Rohrer, P.A. Salvador, Competitive growth of scrutinyite (α-PbO_2) and rutile polymorphs of SnO_2 on all orientations of columbite $CoNb_2O_6$ substrates, Cryst. Growth Des. 17 (7) (2017) 3929–3939.
[7] C. Zhou, M. De Graef, B. Dabrowski, G.S. Rohrer, P.A. Salvador, Combinatorial substrate epitaxy investigation of polytypic growth of $AEMnO_3$ (AE=Ca, Sr), J. Am. Ceram. Soc. 103 (3) (2020) 2225–2234.
[8] C. Zhou, G.S. Rohrer, M.D. Graef, P.A. Salvador, Epitaxial phase stability of $SrMnO_{3-x}$ films on polycrystalline perovskite substrates, Cryst. Growth Des. 21 (8) (2021) 4547–4555.
[9] S.A. Lee, J.M. Ok, J. Lee, J.Y. Hwang, S. Yoon, S.J. Park, S. Song, J.S. Bae, S. Park, H.N. Lee, W.S. Choi, Epitaxial stabilization of metastable 3C $BaRuO_3$ thin film with ferromagnetic non-Fermi liquid phase, Adv. Electron. Mater. 7 (4) (2021) 2001111.
[10] M. Markelova, R. Nygaard, D. Tsymbarenko, A. Shurkina, A. Abramov, V. Amelichev, A. Makarevich, A. Vasiliev, A. Kaul, Multiferroic h-$LuFeO_3$ thin films on (111) and (100) surfaces of YSZ substrates: An experimental and theoretical study, ACS Appl. Electron. Mater. 3 (2) (2021) 1015–1022.
[11] J.M. Rondinelli, A.S. Eidelson, N.A. Spaldin, Non-d^0 Mn-driven ferroelectricity in antiferromagnetic $BaMnO_3$, Phys. Rev. B 79 (20) (2009) 1–6.
[12] A. Marthinsen, C. Faber, U. Aschauer, N.A. Spaldin, S.M. Selbach, Coupling and competition between ferroelectricity, magnetism, strain, and oxygen vacancies in $AMnO_3$ perovskites, MRS Commun. 6 (3) (2016) 182–191.
[13] M.R. Walden, C.V. Ciobanu, G.L. Brennecka, Stability of epitaxial $BiXO_3$ phases by density-functional theory, APL Mater. 8 (8) (2020) 081106.
[14] P. Mehta, P.A. Salvador, J.R. Kitchin, Identifying potential BO_2 oxide polymorphs for epitaxial growth candidates, ACS Appl. Mater. Interfaces 6 (5) (2014) 3630–3639.
[15] Z. Xu, P. Salvador, J.R. Kitchin, First-principles investigation of the epitaxial stabilization of oxide polymorphs: TiO_2 on (Sr,Ba)TiO_3, ACS Appl. Mater. Interfaces 9 (4) (2017) 4106–4118.
[16] Y. Zhang, A.M. Schultz, L. Li, H. Chien, P.A. Salvador, G.S. Rohrer, Combinatorial substrate epitaxy: A high-throughput method for determining phase and orientation relationships and its application to $BiFeO_3$/TiO_2 heterostructures, Acta Mater. 60 (19) (2012) 6486–6493.
[17] A.M. Schultz, Y. Zhu, S.A. Bojarski, G.S. Rohrer, P.A. Salvador, Eutaxial growth of hematite Fe_2O_3 films on Perovskite $SrTiO_3$ polycrystalline substrates, Thin Solid Films 548 (2013) 220–224.
[18] T. Negas, R.S. Roth, The system $SrMnO_{3-x}$, J. Solid State Chem. 1 (3–4) (1970) 409–418.
[19] T. Negas, R.S. Roth, Phase equilibria and structural relations in the system $BaMnO_{3-x}$, J. Solid State Chem. 3 (3) (1971) 323–339.
[20] K. Uematsu, K. Kuroda, N. Mizutani, M. Kato, Oxygen deficiency induced polymorphs of $BaMnO_{3-x}$, J. Am. Ceram. Soc. 60 (9–10) (1977) 466–467.
[21] K. Kuroda, K. Shinozaki, K. Uematsu, N. Mizutani, M. Kato, Phase relation and oxygen deficiency of $SrMnO_{3-x}$, Nippon Kagaku Kaishi 1977 (11) (1977) 1620–1625.
[22] J.J. Adkin, M.A. Hayward, $BaMnO_{3-x}$ revisited: A structural and magnetic study, Chem. Mater. 19 (4) (2007) 755–762.
[23] Q. Zhou, B.J. Kennedy, Thermal expansion and structure of orthorhombic $CaMnO_3$, J. Phys. Chem. Solids 67 (7) (2006) 1595–1598.
[24] V.M. Goldschmidt, Die Gesetze der Krystallochemie, Naturwissenschaften 14 (21) (1926) 477–485.
[25] E. Langenberg, R. Guzmán, L. Maurel, L. Martínez de Baños, L. Morellón, M.R. Ibarra, J. Herrero-Martín, J. Blasco, C. Magén, P.A. Algarabel, J.A. Pardo, Epitaxial stabilization of the perovskite phase in $(Sr_{1-x}Ba_x)MnO_3$ thin films, ACS Appl. Mater. Interfaces 7 (43) (2015) 23967–23977.
[26] R.N. Song, M.H. Hu, X.R. Chen, J.D. Guo, Epitaxial growth and thermostability of cubic and hexagonal $SrMnO_3$ films on $SrTiO_3$ (111), Front. Phys. 10 (3) (2015) 321–326.
[27] P. Agrawal, J. Guo, P. Yu, C. Hébert, D. Passerone, R. Erni, M.D. Rossell, Strain-driven oxygen deficiency in multiferroic $SrMnO_3$ thin films, Phys. Rev. B 94 (10) (2016) 104101.
[28] C. Ricca, I. Timrov, M. Cococcioni, N. Marzari, U. Aschauer, Self-consistent site-dependent DFT+U study of stoichiometric and defective $SrMnO_3$, Phys. Rev. B 99 (9) (2019) 094102.
[29] R. Søndenå, S. Stølen, P. Ravindran, T. Grande, N.L. Allan, Corner- versus face-sharing octahedra in $AMnO_3$ perovskites (A=Ca, Sr, and Ba), Phys. Rev. B 75 (18) (2007) 184105.
[30] L. Maurel, N. Marcano, T. Prokscha, E. Langenberg, J. Blasco, R. Guzmán, A. Suter, C. Magén, L. Morellón, M.R. Ibarra, J.A. Pardo, P.A. Algarabel, Nature of antiferromagnetic order in epitaxially strained multiferroic $SrMnO_3$ thin films, Phys. Rev. B 92 (2) (2015) 024419.
[31] C. Becher, L. Maurel, U. Aschauer, M. Lilienblum, C. Magén, D. Meier, E. Langenberg, M. Trassin, J. Blasco, I.P. Krug, P.A. Algarabel, N.A. Spaldin, J.A. Pardo, M. Fiebig, Strain-induced coupling of electrical polarization and structural defects in $SrMnO_3$ films, Nat. Nanotechnol. 10 (8) (2015) 661–665.
[32] J.W. Guo, P.S. Wang, Y. Yuan, Q. He, J.L. Lu, T.Z. Chen, S.Z. Yang, Y.J. Wang, R. Erni, M.D. Rossell, V. Gopalan, H.J. Xiang, Y. Tokura, P. Yu, Strain-induced ferroelectricity and spin-lattice coupling in $SrMnO_3$ thin films, Phys. Rev. B 97 (23) (2018) 235135.
[33] G. Gökolu, H. Yildirim, Electronic structure and surface properties of cubic perovskite oxide $BaMnO_3$, Comput. Mater. Sci. 50 (3) (2011) 1212–1216.
[34] N. Hamdad, The ground states properties and the spin effect on the cubic and hexagonal perovskite manganese oxide $BaMnO_3$: GGAU calculation, Phys. B Condens. Matter 406 (6–7) (2011) 1194–1203.
[35] H. An, Y.G. Choi, Y.R. Jo, H.J. Hong, J.K. Kim, O. Kwon, S. Kim, M. Son, J. Yang, J.C. Park, H. Choi, J. Lee, J. Song, M.H. Ham, S. Ryu, Y. Kim, C.W. Bark, K.T. Ko, B.J. Kim, S. Lee, Experimental realization of strain-induced room-temperature ferroelectricity in $SrMnO_3$ films via selective oxygen annealing, NPG Asia Mater. 13 (69) (2021) 1–10.
[36] L. Maurel, N. Marcano, E. Langenberg, R. Guzmán, T. Prokscha, C. Magén, J.A. Pardo, P.A. Algarabel, Engineering the magnetic order in epitaxially strained $Sr_{1-x}Ba_xMnO_3$ perovskite thin films, APL Mater. 7 (4) (2019) 041117.
[37] A. Edström, C. Ederer, Magnetic and ferroelectric properties of $Sr_{1-x}Ba_xMnO_3$ from first principles, Phys. Rev. Res. 2 (4) (2020) 043183.
[38] J.H. Lee, K.M. Rabe, Epitaxial-strain-induced multiferroicity in $SrMnO_3$ from first principles, Phys. Rev. Lett. 104 (20) (2010) 207204.
[39] H. Chen, A.J. Millis, Phase diagram of $Sr_{1-x}Ba_xMnO_3$ as a function of chemical doping, epitaxial strain, and external pressure, Phys. Rev. B 94 (16) (2016) 165106.
[40] P. Giannozzi, S. Baroni, N. Bonini, M. Calandra, R. Car, C. Cavazzoni, D. Ceresoli, G.L. Chiarotti, M. Cococcioni, I. Dabo, A. Dal Corso, S. de Gironcoli, S. Fabris, G. Fratesi, R. Gebauer, U. Gerstmann, C. Gougoussis, A. Kokalj, M. Lazzeri, L. Martin-Samos, N. Marzari, F. Mauri, R. Mazzarello, S. Paolini, A. Pasquarello, L. Paulatto, C. Sbraccia, S. Scandolo, G. Sclauzero, A.P. Seitsonen, A. Smogunov, P. Umari, R.M. Wentzcovitch, QUANTUM ESPRESSO: A modular and open-source software project for quantum simulations of materials, J. Phys.: Condens. Matter 21 (39) (2009) 395502.
[41] J.P. Perdew, K. Burke, M. Ernzerhof, Generalized gradient approximation made simple, Phys. Rev. Lett. 77 (18) (1996) 3865–3868.
[42] P.E. Blöchl, Projector augmented-wave method, Phys. Rev. B 50 (24) (1994) 17953.
[43] A. Dal Corso, Pseudopotentials periodic table: From H to Pu, Comput. Mater. Sci. 95 (2014) 337–350.
[44] H. Sakai, J. Fujioka, T. Fukuda, D. Okuyama, D. Hashizume, F. Kagawa, H. Nakao, Y. Murakami, T. Arima, A.Q. Baron, Y. Taguchi, Y. Tokura, Displacement-type ferroelectricity with off-center magnetic ions in perovskite $Sr_{1-x}Ba_xMnO_3$, Phys. Rev. Lett. 107 (13) (2011) 137601.
[45] R.F. Farrow, The stabilization of metastable phases by epitaxy, J. Vac. Sci. Technol. B Microelectron. Nanom. Struct. 1 (1983) 222–228.
[46] M. Quillec, H. Launios, M.C. Joncour, Liquid phase epitaxy of unstable alloys: Substrate-induced stabilization and connected effects, J. Vac. Sci. Technol. B Microelectron. Process. Phenom. 1 (1983) 238–242.

[47] N.E. Singh-Miller, N. Marzari, Surface energies, work functions, and surface relaxations of low-index metallic surfaces from first principles, Phys. Rev. B 80 (23) (2009) 235407.

[48] B. J. Morgan, Javier Carrasco, Gilberto Teobaldi, Variation in surface energy and reduction drive of a metal oxide lithium-ion anode with stoichiometry: A DFT study of lithium titanate spinel surfaces, J. Mater. Chem. A 4 (43) (2016) 17180–17192.

[49] J. Wang, S.Q. Wang, Surface energy and work function of fcc and bcc crystals: Density functional study, Surf. Sci. 630 (2014) 216–224.

[50] G. Hautier, S.P. Ong, A. Jain, C.J. Moore, G. Ceder, Accuracy of density functional theory in predicting formation energies of ternary oxides from binary oxides and its implication on phase stability, Phys. Rev. B 85 (15) (2012) 155208.

[51] M.B. Nielsen, D. Ceresoli, P. Parisiades, V.B. Prakapenka, T. Yu, Y. Wang, M. Bremholm, Phase stability of the $SrMnO_3$ hexagonal perovskite system at high pressure and temperature, Phys. Rev. B 90 (21) (2014) 214101.

[52] A.K. Mandal, G. Panchal, S. Chowdhury, A. Jana, R.J. Choudhary, D.M. Phase, Electronic and magnetic properties of stoichiometric and off-stoichiometric $SrMnO_3$ thin films, J. Supercond. Nov. Magn. 33 (2020) 1633–1636.

[53] A.K. Mandal, A. Jana, B.K. De, N. Patra, P. Rajput, V. Sathe, S.N. Jha, R.J. Choudhary, D.M. Phase, Understanding defect-mediated cubic to hexagonal topotactic phase evolution in $SrMnO_3$ thin films and associated magnetic and electronic properties, Phys. Rev. B 103 (2021) 195110.

[54] M.K. Lee, C.B. Eom, J. Lettieri, I.W. Scrymgeour, D.G. Schlom, W. Tian, X.Q. Pan, P.A. Ryan, F. Tsui, Epitaxial thin films of hexagonal $BaRuO_3$ on (001) $SrTiO_3$, Appl. Phys. Lett. 78 (3) (2001) 329–331.

[55] K.K. Ghose, A. Bayon, A.J. Page, First-principles thermochemical properties of hexagonal and cubic phase $BaMnO_3$, Mater. Today Commun. 31 (2022) 103453.

[56] A. Kumar, M. Kumar, R.P. Singh, P.K. Singh, Opto-electronic, magnetic, thermodynamic and thermoelectric properties of cubic perovskite $SrMnO_3$: A first principle based spin polarized calculation, Solid State Commun. 324 (2021) 114139.

[57] S.J. Heo, A. Zakutayev, Combinatorial screening of the crystal structure in Ba-Sr-Mn-Ce perovskite oxides with ABO_3 stoichiometry, J. Mater. Chem. A 9 (2021) 21032–21043.

[58] D.L. Olmsted, E.A. Holm, S.M. Foiles, Survey of computed grain boundary properties in face-centered cubic metals—II: Grain boundary mobility, Acta Mater. 57 (13) (2009) 3704–3713.

[59] H.-S. Lee, T. Mizoguchi, T. Yamamoto, S.J.L. Kang, Y. Ikuhara, Characterization and atomic modeling of an asymmetric grain boundary, Phys. Rev. B 84 (19) (2011) 195319.

[60] S. Ratanaphan, D.L. Olmsted, V.V. Bulatov, E.A. Holm, A.D. Rollett, G.S. Rohrer, Grain boundary energies in body-centered cubic metals, Acta Mater. 88 (2015) 346–354.

[61] T. Yokoi, Y. Kondo, K. Ikawa, A. Nakamura, K. Matsunaga, Stable and metastable structures and their energetics of asymmetric tilt grain boundaries in MgO: A simulated annealing approach, J. Mater. Sci. 56 (4) (2021) 3183–3196.

[62] Y. Zhang, E.D. Hansen, T. Harbison, S. Masengale, J. French, L. Aagesen, A molecular dynamics survey of grain boundary energy in uranium dioxide and cerium dioxide, J. Am. Ceram. Soc. 105 (6) (2022) 4471–4486.

[63] C. Tao, D. Mutter, D.F. Urban, C. Elsässer, Electrostatic treatment of charged interfaces in classical atomistic simulations, Modelling Simul. Mater. Sci. Eng. 30 (5) (2022) 055004.

[64] D. Mutter, C. Tao, D.F. Urban, C. Elsässer, Formation energy profiles of oxygen vacancies at grain boundaries in perovskite-type electroceramics, Adv. Eng. Mater. (2023) 2201847.

[65] J.E. Greene, Thin film nucleation, growth, and microstructural evolution: An atomic scale view, in: Handb. Depos. Technol. Film. Coatings Sci. Appl. Technol., William Andrew Publishing, 2010, pp. 554–620.

[66] L. Rørmark, A.B. Mørch, K. Wiik, S. Stølen, T. Grande, Enthalpies of oxidation of $CaMnO_{3-\delta}$, $Ca_2MnO_{4-\delta}$ and $SrMnO_{3-\delta}$ - deduced redox properties, Chem. Mater. 13 (11) (2001) 4005–4013.

[67] L. Rørmark, K. Wiik, S. Stølen, T. Grande, Oxygen stoichiometry and structural properties of $La_{1-x}A_xMnO_{3\pm\delta}$ (A=Ca or sr and $0 \leq x \leq 1$), J. Mater. Chem. 12 (4) (2002) 1058–1067.

[68] R. Søndenå, S. Stølen, P. Ravindran, T. Grande, Heat capacity and lattice dynamics of cubic and hexagonal $SrMnO_3$: Calorimetry and density functional theory simulations, Phys. Rev. B 75 (2007) 214307.

[69] B. Dabrowski, O. Chmaissem, J. Mais, S. Kolesnik, J.D. Jorgensen, S. Short, Tolerance factor rules for $Sr_{1-x-y}Ca_xBa_yMnO_3$ perovskites, J. Solid State Chem. 170 (1) (2003) 154–164.

[70] H. Wang, V. Srot, X. Jiang, M. Yi, Y. Wang, H. Boschker, R. Merkle, R.W. Stark, J. Mannhart, P.A. van Aken, Probing charge accumulation at $SrMnO_3/SrTiO_3$ heterointerfaces via advanced electron microscopy and spectroscopy, ACS Nano 14 (10) (2020) 12697–12707.

[71] M. Kaviani, U. Aschauer, Surface and interface effects in oxygen-deficient $SrMnO_3$ thin films grown on $SrTiO_3$, Phys. Chem. Chem. Phys. 24 (6) (2022) 3951–3957.

[72] G.L. Yuan, A. Uedono, Behavior of oxygen vacancies in $BiFeO_3/SrRuO_3/SrTiO_3(100)$ and $DyScO_3(100)$ heterostructures, Appl. Phys. Lett. 94 (13) (2009) 132905.

[73] A. Marthinsen, T. Grande, S.M. Selbach, Microscopic link between electron localization and chemical expansion in $AMnO_3$ and $ATiO_3$ perovskites (A=Ca, Sr, Ba), J. Phys. Chem. C 124 (24) (2020) 12922–12932.

[74] V.I. Anisimov, J. Zaanen, O.K. Andersen, Band theory and Mott insulators: Hubbard U instead of Stoner I, Phys. Rev. B 44 (3) (1991) 943.

[75] G.C. Moore, M.K. Horton, A.M. Ganose, M. Siron, K.A. Persson, High-throughput determination of Hubbard U and Hund J values for transition metal oxides via linear response formalism, 2022.

[76] K. Lee, R.A. Flores, Y. Liu, B.Y. Wang, Y. Hikita, R. Sinclair, M. Bajdich, H.Y. Hwang, Epitaxial stabilization and oxygen evolution reaction activity of metastable columbite iridium oxide, ACS Appl. Energy Mater. 4 (4) (2021) 3074–3082.

[77] K.R. Gann, C.S. Chang, M.C. Chang, D.R. Sutherland, A.B. Connolly, D.A. Muller, R.B. Van Dover, M.O. Thompson, Initial nucleation of metastable γ-Ga_2O_3 during sub-millisecond thermal anneals of amorphous Ga_2O_3, Appl. Phys. Lett. 121 (6) (2022) 062102.

[78] H. Zhang, J.F. Banfield, Thermodynamic analysis of phase stability of nanocrystalline titania, J. Mater. Chem. 8 (9) (1998) 2073–2076.

[79] Y. Li, T. Ishigaki, Thermodynamic analysis of nucleation of anatase and rutile from TiO_2 melt, J. Cryst. Growth 242 (3–4) (2002) 511–516.

[80] D. Rafieian, W. Ogieglo, T. Savenije, R.G. Lammertink, Controlled formation of anatase and rutile TiO_2 thin films by reactive magnetron sputtering, AIP Adv. 5 (9) (2015) 097168.

[81] A.R. Korpi, S. Rezaee, C. Luna, lu, A. Arman, A. Ahmadpourian, Influence of the oxygen partial pressure on the growth and optical properties of RF-sputtered anatase TiO_2 thin films, Results Phys. 7 (2017) 3349–3352.

Supplemental Information for Computationally Guided Epitaxial Synthesis of (Sr/Ba)MnO_3 Films on (Sr/Ba)TiO_3 Substrates

Catherine Zhou, Gregory S. Rohrer, Paul A. Salvador

Department of Materials Science and Engineering, Carnegie Mellon University, 5000 Forbes Ave., Pittsburgh, Pennsylvania 15213, USA. *paulsalvador@cmu.edu

Abstract

This document provides Supplementary Information to the main text. Section S1 describes how surfaces used in computations were generated from starting surfaces of each polytype. Section S2 describes an experimental investigation of $BaMnO_3$ stability in the $4H$ and $2H$ structures on $3C$ $SrTiO_3$ single crystals by changing the overall pressure (and the partial pressure of oxygen) during deposition. Section S3 presents the computations of bulk stability for two values of oxygen vacancy concentration. Section S4 describes the impact of adding the Hubbard U term to DFT energy calculations. References used in this supplemental section are given at the end.

S1 Unit Cell Transformations

Transformation of bulk and interface unit cells from the default (100) orientation into different orientations followed the approach explained in the tutorial, "How to Prepare an Input File for Surface Calculations" by Emre S. Tasci.[1] All transformations were done in VESTA,[2] a three-dimensional crystal structure visualization software. The starting $3C$ and

$4H$ structures are presented as $3C$ (100) or $4H$ (00.1) (hexagonal notation, only used in this section), and are represented by the identity matrix:

$$I = \begin{bmatrix} 1 & 0 & 0 \\ 0 & 1 & 0 \\ 0 & 0 & 1 \end{bmatrix}$$

To generate a new orientation where the desired plane normal is parallel with the c-axis, the identity matrix is multiplied by a transformation matrix, M. Each column in M are the directions of the new basis vectors (with respect I) and are all orthogonal to each other. For the orientation relationships (ORs) presented in Table 1, the following matrix transformations were employed:

- $3C$ (100) to $3C$ (110)

$$M = \begin{bmatrix} 0 & -1 & 1 \\ 0 & 1 & 1 \\ -1 & 0 & 0 \end{bmatrix}$$

- $3C$ (100) to $3C$ (111)

$$M = \begin{bmatrix} -1 & -1 & 1 \\ 1 & -1 & 1 \\ 0 & 2 & 1 \end{bmatrix}$$

- $4H$ (00.1) to $4H$ (001) and $2H$ (00.1) to $2H$ (001)

Please note the difference in notation between hexagonal and orthorhombic orienta-

tions. The dot is implied everywhere else where the hexagonal structure is mentioned. M transforms a set of hexagonal basis vectors to a set of orthorhombic basis vectors.

$$M = \begin{bmatrix} 1 & 1 & 0 \\ 0 & 2 & 0 \\ 0 & 0 & 1 \end{bmatrix}$$

The resulting exposed planes, looking down the c direction, are shown in Figure S1.

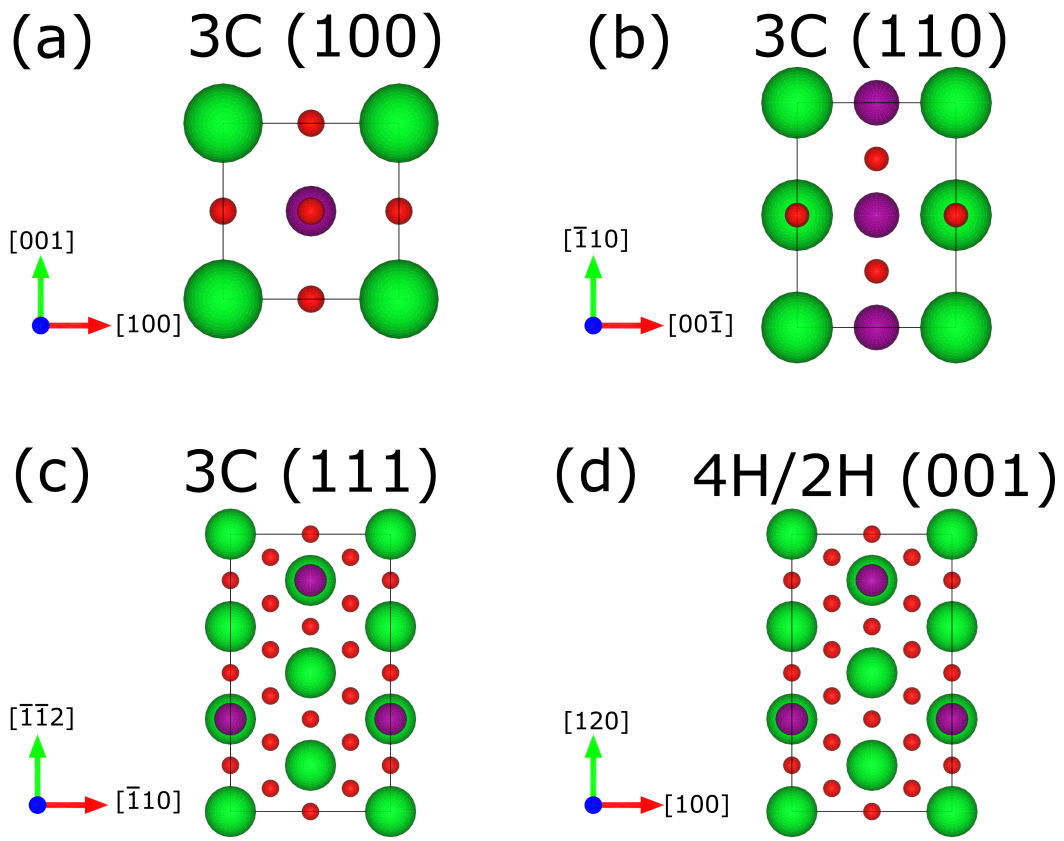

Figure S1: Looking down the c direction for the (a) 3C (100) cell, (b) 3C (110) face cell, (c) 3C (111) cell, and (d) 4H/2H (001) cell. Green, purple, and red balls represent Sr/Ba, Mn, and O atoms, respectively.

S2 $BaMnO_3$ on $SrTiO_3$ (111)

$BaMnO_3$ films approximately 150 nm thick were deposited using pulsed laser deposition (PLD), with a KrF laser (248 nm) on $SrTiO_3$ (111) substrates.[3] A $4H$ $BaMnO_3$ target was synthesized using standard solid-state techniques. Stoichiometric amounts of $BaCO_3$ and MnO_2 were mixed in ethanol, ball-milled overnight, hand-ground, and uniaxially pressed to pressure $> 10,000$ psi. The resulting target was sintered at 900, 1200, and 1500 °C for 12, 12, and 15 h, respectively. In between each sintering step, the target was reground. A small amount of powder was used to monitor phase progression using X-ray diffraction (XRD). The target was likely oxygen deficient, as oxygen stoichiometry was not controlled during synthesis or measured afterwards.

Two deposition pressures were tested while all other parameters were kept the same. One film was deposited in a total pressure of 2×10^{-3} Torr of pure O_2 and one in a total pressure of 3×10^{-5} Torr with no process gas (i.e, in the chamber background pressure). The oxygen partial pressure for the film deposited under background pressure was not controlled or measured, but it is at least equal to or less than 3×10^{-5} Torr. The substrate temperature was kept at 850 °C. The laser frequency and energy density were kept at 2 Hz and 1 J/cm^2, respectively. After deposition, films were cooled in 200 Torr of pure O_2. These conditions are relatively standard values for growth of similar phases.[3,4] The growth rate was measured from a $BaMnO_3$ film on (111) MgO in the first set of conditions, with 2×10^{-3} Torr of pure O_2, and the films were then deposited for 15,000 pulses each. Differences in deposition rate for the second set of conditions were not investigated or measured.

XRD pattern of the film deposited in 2×10^{-3} Torr of pure O_2 is shown in Fig. S2a. Two main film peaks are attributed to the (002) and (004) locations of the $2H$ $BaMnO_3$ phase. The (002) peak is located at a 2Θ position of 37.6° ($c \approx 4.78$ Å). The (004) peak is located at 79.8° ($c \approx 4.80$ Å). In bulk, the expected c-axis lattice parameter is 4.81 Å.[5,6] The small

percent difference between the film and bulk lattice parameters is within experimental error, indicating that the film is relaxed. Asterisks are shown for the forbidden (001) and (003) peaks, which could be attributed to the presence of stacking faults (cubic stacking layers or some $4H$-like layers), which result in incomplete cancellation of intensity.

XRD pattern of the film deposited in the chamber background pressure is shown in Fig. S2b. Four film peaks are attributed as belonging to the $4H$ phase. The $(002n)$ peaks (equivalent c lattice parameter from the peak) are located at 19.2° ($c \approx 9.23$ Å), 39.0 ° ($c \approx 9.23$ Å), 60.2 ° ($c \approx 9.21$ Å), and 83.8° ($c \approx 9.22$ Å) for n=1, 2, 3, and 4, respectively. The bulk c-axis lattice parameter for the $4H$ phase is 9.32 Å, and the film's value is 1.07% smaller than that. The intensity of the primary peaks are similar between the two phases, indicating the thicknesses are not orders of magnitude different. We expect the film to be relaxed at such thicknesses, like the $2H$ was. The slight variation between the relaxed film and bulk lattice parameters was not investigated further, but may be due to slight stoichiometry or internal stress variations from depositing under the chamber background pressure without process gas. The difference is not likely an epitaxial strain, as the expected in-plane strain should be compressive, resulting in an out-of-plane expansion, not the slight contraction observed.

Both of these hexagonal phases form a coherent interface with the eutactic $3C$ (111) plane of $SrTiO_3$, and their energetic differences are described in the main text. The supplemental results are consistent with the idea that thermodynamic parameters, here oxygen activity, influence phase formation of the hexagonal polytypes.

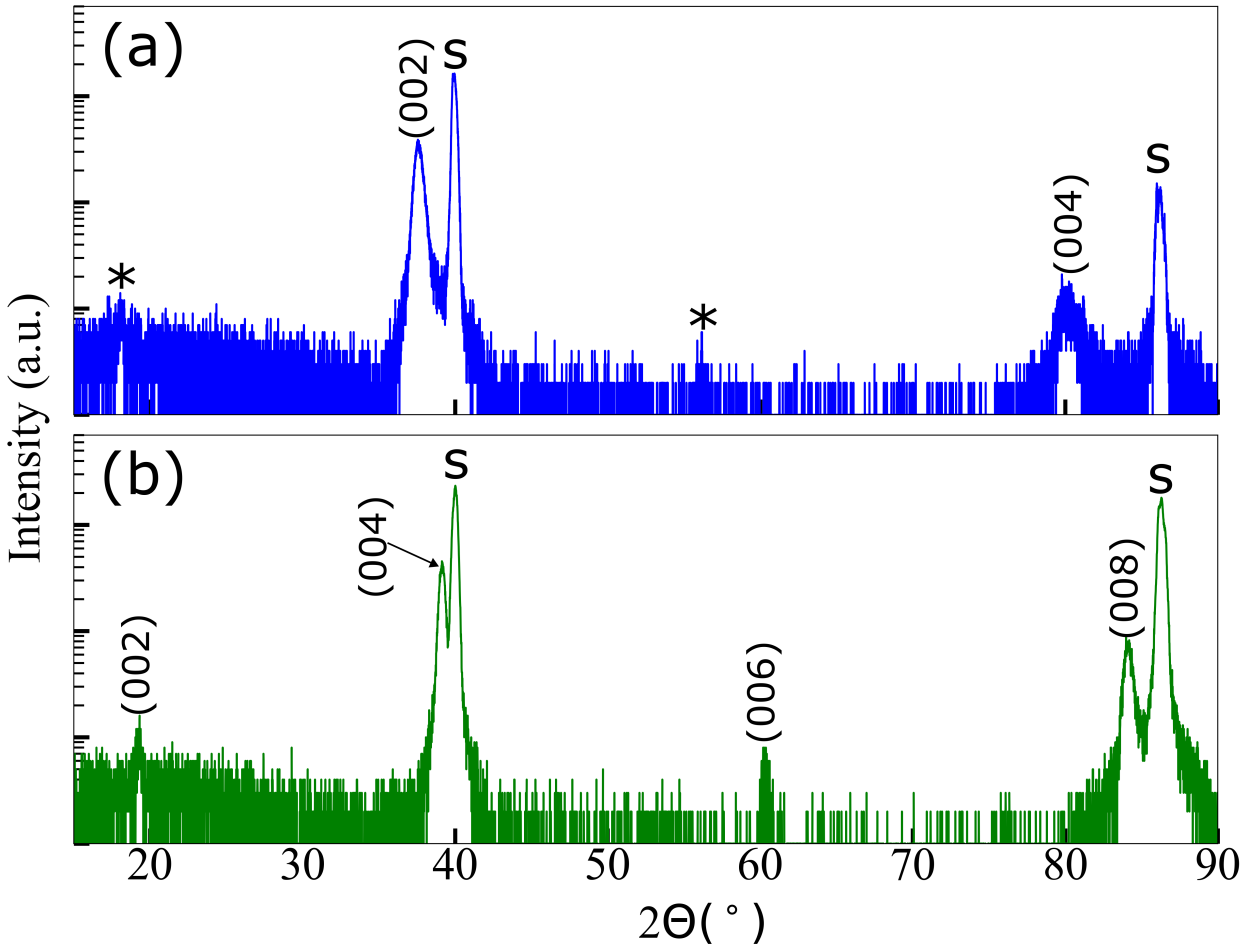

Figure S2: XRD patterns of 150 nm $BaMnO_3$ films on $SrTiO_3$ (111) substrates using (a) 2×10^{-3} Torr pure O_2 and (b) 3×10^{-5} Torr (background pressure). The films are indexed as (a) $2H$ and (b) $4H$. s denotes the location of the substrate peaks. Asterisks mark the location of forbidden peaks in the $2H$ phase.

S3 Oxygen Deficient $SrMnO_{3-\delta}$

Bulk formation energy values were computed for two oxygen-deficient compositions of $SrMnO_{3-\delta}$, $\delta = 0.25$ and 0.5. Similarly to Eq. 2, the formation energy is calculated by subtracting the total energy of the non-stoichiometric compound by its binary compounds, and dividing by number of formula units (1 f.u. = 5 atoms). For $3C$ and $4H$ $SrMnO_{2.75}$ the equation is:

$$\Delta E_{b,Sr_4Mn_4O_{11}} = \frac{1}{4}(E_{Sr_4Mn_4O_{11}} - 2 * E_{MnO_2} - E_{Mn_2O_3} - 4 * E_{SrO}) \tag{1}$$

For $3C$ $SrMnO_{2.5}$, the equation is:

$$\Delta E_{b,Sr_2Mn_2O_5} = \frac{1}{2}(E_{Sr_2Mn_2O_5} - E_{Mn_2O_3} - 2 * E_{SrO}) \tag{2}$$

while for $4H$ $SrMnO_{2.5}$, the equation is:

$$\Delta E_{b,Sr_4Mn_4O_{11}} = \frac{1}{4}(E_{Sr_4Mn_4O_{11}} - 2 * E_{Mn_2O_3} - 4 * E_{SrO}) \tag{3}$$

For $3C$ $SrMnO_{2.75}$, a $2\times2\times1$ supercell containing four formula units was constructed and one random oxygen atom was removed. For $3C$ $SrMnO_{2.5}$, a $2 \times 1 \times 1$ supercell containing two formula units was constructed and one random oxygen atom removed. For $4H$ $SrMnO_3$, the unit cell already contains 4 formula units, so one oxygen atom was removed to create $4H$ $SrMnO_{2.75}$ and two random oxygen atoms were removed to generate $4H$ $SrMnO_{2.5}$. Energy values computed as such were then normalized to the number of formula units assuming no oxygen atoms were removed. The results for the bulk formation energies are presented in Table S1.

When comparing the ΔE_b values between $SrMnO_3$ polytypes, the $3C$ phase is always higher in energy regardless of oxygen content. For $SrMnO_3$, the difference in bulk formation

Table S1: Bulk Formation Energy Values for $SrMnO_{3-\delta}$.

δ	ΔE_b^{3C} (kJ/mol)	V^{3C} (Å^3/f.u.)	ΔE_b^{4H} (kJ/mol)	V^{4H} (Å^3/f.u.)	$\Delta\Delta E_b^{3C-4H}$
0	-50.73	55.00	-76.29	58.05	25.56
0.25	-47.27	55.53	-70.21	57.63	22.94
0.5	-31.05	54.73	-55.59	56.60	24.54

energy, $\Delta\Delta E_b^{3C-4H}$, is 25.56 kJ/mol. When $\delta = 0.25$ or 0.5, these values are 22.94 and 24.54 kJ/mol, respectively. Columns 3 and 5 show the volume per formula unit for each of the stoichiometry and non-stoichiometric cells. It was expected that the removal of an oxygen atom would increase the volume, but this only occurs when $\delta = 0.25$. We did not explore if removing other symmetrically inequivalent oxygen atoms changed the volumes and energy values, nor if larger supercells or specific ordering also impacted them. These values should be considered coarse approximations. That the bulk energy differences between polymorphs are a bit lower for the oxygen deficient phases is consistent with the idea that the $3C$ phase is less unstable at lower oxygen partial pressures, but it does not support an overall change in stability with oxygen content. As discussed in the main text, all of these energy differences are near the the 20 kJ/mol approximation for which epitaxial stabilization is likely to succeed.

S4 DFT+U Correction

To assess whether the prior results of epitaxial polymorph competition for $SrMnO_3$ were affected by the DFT methodology, further computational investigations were carried out using an effective Hubbard U correction of 3 eV on the Mn $3d$ electrons.[7] This value has been shown to accurately reproduce the density of states and G-type antiferromagnetic order for $CaMnO_3$.[8,9]

Table S2 shows the bulk, strain, and interface energy values for $SrMnO_3$ polytypes on (111) $SrTiO_3$ using U=3 eV. All values are generally similar to those calculated without the inclusion of the U parameter, except for σ_{int} for the $3C$ phase, which is increased by 89% using the U correction. This greatly penalizes the $3C$ phase compared to the $4H$, but does not lead to a significant change in the final ΔE^{3C-4H} value.

Table S3 shows the thermodynamic terms relevant to epitaxial nucleation of $SrMnO_3$ on $SrTiO_3$ using U=3 eV. The difference in volumetric energy at 1 nm decreases from 0.858 J/m^2 to 0.775 J/m^2 with the addition of the U parameter, decreasing $4H$ bulk stability. The difference in interface energy increases from -0.119 J/m^2 to -0.099 J/m^2, slightly increasing the penalty for the $3C$ phase. For the strain energy, the U correction penalizes the $3C$ with a higher strain energy on $SrTiO_3$ (111), and decreases it for the $4H$ phase. The total energetic difference for a 1 nm film with competing polymorphs decreases from 0.739 J/m^2 to 0.676 J/m^2. Overall, the inclusion of U in this system does not drastically change epitaxial stability between $3C$ and $4H$ $SrMnO_3$, at least on (111) $SrTiO_3$.

Table S2: Bulk, Strain, and Interface Energy of $SrMnO_3$ Polytypes on (111) $SrTiO_3$ (J/m^2), with Hubbard U Correction.

$SrMnO_3$ Polytype	ΔE_b (kJ/mol)	ΔE_w (kJ/mol)	σ_{int} (J/m^2)
3C	-55.52	15.36	0.017
4H	-77.12	7.50	0.116

Table S3: Thermodynamic Terms Relevant to Epitaxial Nucleation of $SrMnO_3$ Polytypes on (111) $SrTiO_3$ (J/m^2) at 1 nm, with $U = 3$ eV.

$\Delta E_{b+w}^{3C-SMO}d$	$\Delta E_{b+w}^{4H-SMO}d$	$\Delta\Delta E_{b+w}^{3C-4H}d$	$\Delta\sigma_{int}^{3C-4H}$	ΔE^{3C-4H}
-1.241	-2.016	0.775	-0.099	0.676

References

(1) Tasci, E. S. How to Prepare an Input File for Surface Calculations. *online*.

(2) Momma, K.; Izumi, F. VESTA: a three-dimensional visualization system for electronic and structural analysis. *J. Appl. Crystallogr.* **2008**, *41*, 653–658.

(3) Zhou, C.; Rohrer, G. S.; Graef, M. D.; Salvador, P. A. Epitaxial Phase Stability of $SrMnO_{3-x}$ Films on Polycrystalline Perovskite Substrates. *Cryst. Growth Des.* **2021**, *21*, 4547–4555.

(4) Zhou, C.; De Graef, M.; Dabrowski, B.; Rohrer, G. S.; Salvador, P. A. Combinatorial substrate epitaxy investigation of polytypic growth of $AEMnO_3$ (AE= Ca, Sr). *J. Am. Ceram. Soc.* **2020**, *103*, 2225–2234.

(5) Negas, T.; Roth, R. S. Phase equilibria and structural relations in the system $BaMnO_{3-x}$. *J. Solid State Chem.* **1971**, *3*, 323–339.

(6) Cussen, E. J.; Battle, P. D. Crystal and magnetic structures of 2H $BaMnO_3$. *Chem. Mater.* **2000**, *12*, 831–838.

(7) Marthinsen, A.; Faber, C.; Aschauer, U.; Spaldin, N. A.; Selbach, S. M. Coupling and competition between ferroelectricity, magnetism, strain, and oxygen vacancies in $AMnO_3$ perovskites. *MRS Commun.* **2016**, *6*, 182–191.

(8) Jung, J. H.; Kim, K. H.; Eom, D. J.; Noh, T. W.; Choi, E. J.; Yu, J.; Kwon, Y. S.; Chung, Y. Determination of electronic band structures of $CaMnO_3$ and $LaMnO_3$ using optical-conductivity analyses. *Phys. Rev. B* **1997**, *55*, 15489.

(9) Hong, J.; Stroppa, A.; Añiguez, J.; Picozzi, S.; Vanderbilt, D. Spin-phonon coupling effects in transition-metal perovskites: A DFT+U and hybrid-functional study. *Phys. Rev. B* **2012**, *85*, 054417.